Study of n-type Amorphous Silicon Alloy as the Anode in Li-ion Batteries

Author	:	Shihao Wang
Student ID	:	4811909
Date	:	17-09-2020
Departments	:	PVMD group, EWI, TUDelft Material Science and Engineering, 3ME, TUDelft SEE group, AS, TUDelft
Supervisor.	:	Dr. René van Swaaij Dr. Yaiza Gonzalez Garcia
Master's Programme	:	Material Science and Engineering
Credits	:	40EC

Page intentionally left blank

Abstract

In recent years, the world has witnessed a dramatic advancement in sustainable energy development. Due to the inconsistent supply of such energy, a more efficient energy storage method is in need.

Among many options, lithium-ion battery stands out due to its lightweight, high energy density, and high discharge potential. Currently, the most commonly adapted anode materials in lithium-ion batteries are carbon-based, most often graphite. It shows a layered structure that can be used to store Li^+ ions based on the intercalation and de-intercalation mechanism. Although this material is stable and successfully commercialized, due to its low specific capacity efforts have been put into searching other potential anode materials. Potential materials are aluminum, tin, and silicon. Among them, silicon shows an ultra-high (theoretical) specific capacity that is 12 times higher than that of carbon. However, the volume taken up by the material increases by about 300% upon lithiation and de-lithiation. Hence, silicon anodes show a poor capacity retention ability comparing to its graphite counterpart.

In this work, by using a silicon alloy, we aim to alleviate the effects of volume expansion of Si by introducing alloying species and by providing a porous structure. In this work it is demonstrated that this material structure is able to absorb the expansion, while still rendering a high specific capacity. Silicon alloy samples over a wide range of alloy concentration and porosity were synthesized using PECVD. Samples were assembled into pouch-cells and coin-cells and tests were performed to compare the battery performance of each sample. A FEM model was built, enabling more investigation opportunities. Together with the experiments, they revealed how alloy concentration and porosity influence the specific capacity and cycling ability of the anode.

Acknowledgement

First I would like to express my gratitude to Dr.Rene van Swaaij for his immense support. He has been helping me from start to end no effort spared. He has influenced me with his critical attitudes in solving problems and his focus on details. I have learned so much, both scientifically and in how to elaborate my points logically and understandably.

Then I would like to thank Dr.Yaiza Garcia for being my supervisor and helping me coordinating many measurements that are essential for this work, and for helping me preparing the graduation procedure.

Dr. Zhalong Li, Martijn Tijssen, Kees Kwakernaak have assisted me in carrying out many characterizations and battery tests. They also provide me with many professional insights regarding experimental strategy and data analysis, keeping the project going smoothly, I'm very thankful for them.

I would also like to thank Dr. Rudi Santbergen and Dr. Malte Vogt for helping me developing the model every week, the model will not work as well without their guidance. Prof.Dr.ir. Marnix Wagemaker has also provided me with much indicative guidance regarding battery tests, I am very thankful for that.

In addition, I would like to thank Dr. Gregory Pandraud and Dr. Olindo Isabella for introducing me to this project, I would not have the chance to be involved in this fascinating work if it was not for them.

In the end, I would like to say thank you to my colleges in the battery team, Jasper Prins and Nithin Jacob, for their continuous support throughout the project and their suggestions on my experiments, simulations, and presentations, it was a real pleasure working with them.

List of Figures

List of Tables

1.Introduction

As can be seen from Figure 1 (A) [3], over 80% of the global energy sources we are currently using is from coal, gas, and oil, which are not renewable and put high pressure on the environment as well as the well-being of people [1]. This urges us to reach out to more sustainable energy sources with less impact. Both solar and wind energies are legit candidates and Figure 1 (B) shows their shares in the energy sources were increasing during the last 20 years [4] and are expected to continue increasing in the following decades [2]. However, because of the non-stable supply of renewable energy (for example, there is no light during the night), it is of critical importance to find a storage strategy with high efficiency to store the energy for those times of demand.

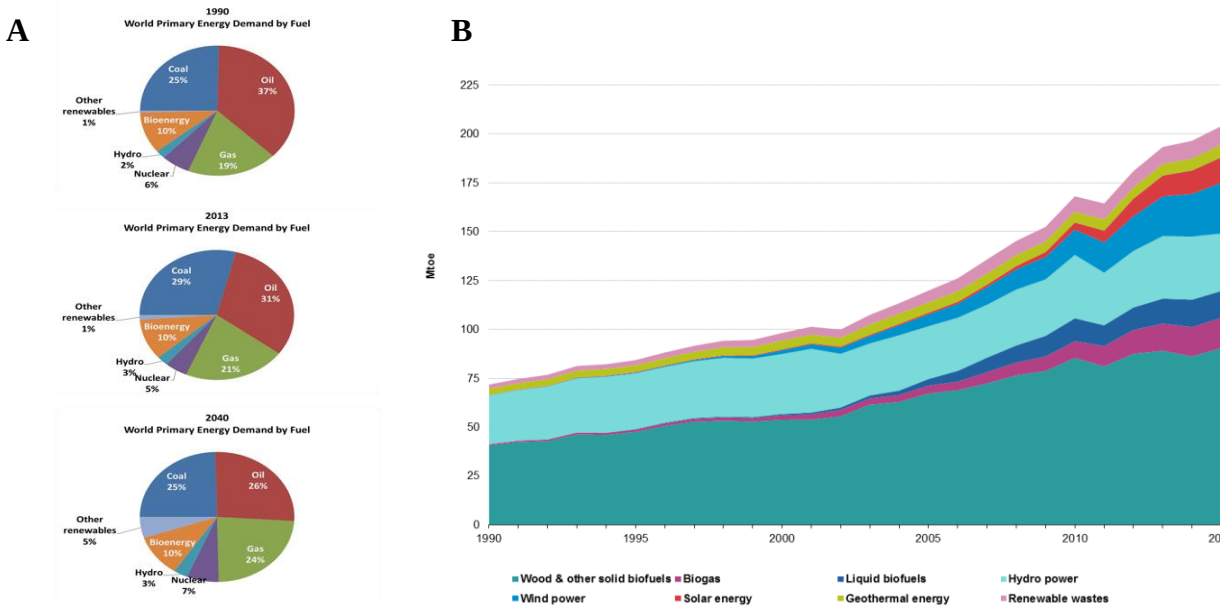

Figure 1. (A) The shares of global energy demand by fuel in 1990, 2013 (the most recent available) and 2040 (projected) [3] and (B) Primary production of energy inside the Europe union from renewable sources, EU-28, 1990-2015 [4].

Up until now many energy storage methods have been invented and put into application, including liquid air energy storage (LAES), pumped heat electrical storage (PHES), superconducting magnet storage (SMS), fuel cells, lithium-ion batteries, (LIBs), etc [5].

Among them, lithium batteries appeared to be an outstanding candidate and are dominating the portable electronics market due to its high gravimetric and volumetric energy density comparing to other energy storage systems [6]. The high energy density mainly results from the high operating voltage 0-4 V thanks to organic electrolytes while the operating voltage was mostly limited to below 2 V in other aqueous systems. Li-ion batteries have been widely adopted in cell phones and laptops and will have a far more pronounced impact when applied in electrical vehicles [7]. There are, some remaining challenges, including increasing the energy density of the batteries, more advanced manufacturing methods to make it more industrial friendly, and of course, with a lower cost [8].

Today, a lithium battery consists of a cathode mostly made of lithium oxide, an anode made of graphite, and electrolyte. It was reported that the properties of the anode can influence the battery performance significantly [9], both in energy density and cyclability of the battery, and this is the main interest of this research.

In the remainder of the introduction, Section 1.1 gives a brief introduction of how lithium-ion battery works. Section 1.2 explains the capacity fade mechanism of the anode in lithium-ion batteries. Section 1.3 gives a brief introduction of the historical development of the anode in the lithium-ion battery, and Section 1.4 shows the previous publication on applying a-SiC_x:H as the anode in lithium-ion battery. Section 1.5 gives the scope and objective of this work.

1.1 Working principle of Lithium-ion battery

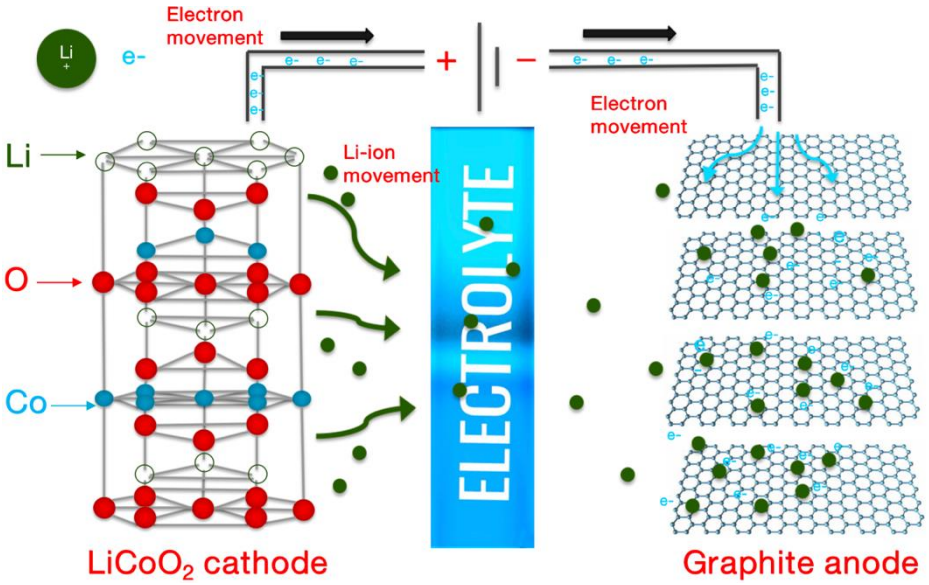

Figure 2. Schematic illustration of the charging process of Li-ion battery.

Like most secondary batteries, lithium-ion batteries mainly consist of a cathode, anode, and electrolyte. Currently, the most commercially popular cathodes are lithium cobalt dioxide ($LiCoO_2$) and lithium iron phosphate ($LiFePO_4$). For anodes, layered graphite is commonly adapted [10]. Lithium in its pure form is highly reactive and has a strong tendency to lose one electron, thus becoming an ion. On the other hand, lithium atoms are very stable in metal oxides, hence the use of lithium oxides in Li-ion batteries. As can be seen in Figure 2, if a power source is connected between cathode and anode, lithium atoms will be separated into lithium ions and electrons, which are then transferred from cathode to anode via the electrolytes and conductive wire, respectively. Holes on the cathode in Figure 2 represent vacancies after lithium atoms have been removed. Separated lithium ions and electrons are then recombined and intercalated between each graphite layer. This is the charging process of the lithium-ion battery.

When the power source is turned off, unstable lithium atoms stored between graphite layers will automatically separate into ions and electrons and return to metal oxides, where they are more

energetically favored. Hence, both electrons and Li^+ ions will flow in the opposite direction as in the charging process. The directional movement of electrons results in electricity.

1.2 Capacity fade mechanism of electrodes

It can be seen from the working principle of a lithium-ion battery, Li^+ ions are the carriers in the battery, the capacity of a battery is determined to a large extent by how many Li^+ ions are available. Hence, one would like to keep every Li^+ ions effective. However, during the charging process when Li+ ions move from the cathode, through the electrolyte, to the anode, the surfaces of Li^+ ions will be covered by the organic solvent in the electrolyte. Li^+ ions can then react with solvent and electrons, forming a solid layer at the surface between electrolyte and anode named the Solid Electrolyte Interface (SEI) layer, as is shown in Figure 3. The formation of this layer consumes Li^+ ions and leads to a capacity decrease. This is the most dominant capacity fade mechanism of the electrodes in a lithium-ion battery.

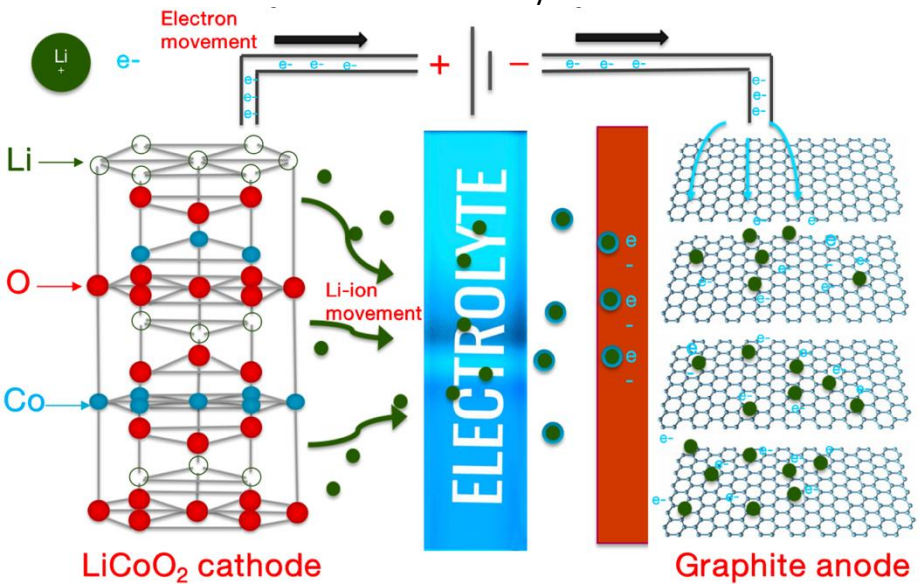

Figure 3. Schematic illustration of the formation mechanism of a solid electrolyte interface (SEI layer).

This reaction between Li^+ ions, electrons and organic solvent can be expressed in the following equations [11]. Here, EC is ethylene carbonate, which is commonly used as the organic solvent in the electrolyte.

$$EC - Li^+ + e^- \longrightarrow C_2H_4OCO_2^- + Li^+ \qquad \text{Equation 1}$$

$$EC - Li^+ + e^- \longrightarrow C_2H_4OCO_2^- + Li^+ \qquad \text{Equation 2}$$

$$EC + 2Li^+ + 2e^- \longrightarrow Li_2CO_3 + C_2H_4 \uparrow \qquad \text{Equation 3}$$

$$EC + 2e^- \longrightarrow OC_2H_4O^{2-}(reactive) + CO \uparrow \qquad \text{Equation 4}$$

This series of reactions is inevitable since the chemical potential of the anode is outside of the electrochemical window of the electrolyte and is usually lower than the reduction potential of the organic solvent (typical 1 V) [12], so this reduction reaction will happen. This is a compromise,

since a lower potential at the anode allows a higher voltage of the battery, but the side reaction forming the SEI layer comes hand in hand.

However, even though the formation of the SEI layer is detrimental to the battery capacity, once it is formed, it is only conductive for Li^+ ions and not for electrons nor organic solvent, which are two reactants in forming the SEI. This protects the anode from the electrolyte and prevents further SEI formation. Understandably, we would like to prevent the SEI formation and save Li^+ ions, but if that is impossible, the second-best choice is to prevent the formed layer from cracking.

1.3 Backgrounds of the anode in lithium-ion battery

1.3.1 Historical development of Lithium-ion battery anode

Among all materials, pure lithium is in theory the most ideal candidate for both cathode and anode material. This is due to its lightweight, high specific capacity, and a high electron transfer ratio. However, lithium is in its pure form a highly reactive alkali metal, meaning violent reactions occur with water under room temperature. This has prevented the wide application of Li for a long time. Later it was proposed that this problem can be alleviated by using 'non-aqueous' electrolytes, like organic solvents [13].

In 1973, lithium anodes were first applied in lithium-ion batteries, with fluorocarbon as the cathode. The electrolyte consisted of lithium salt and organic solvent [14]. One fascinating observation about fluorocarbon was that fluorine atoms seemingly are intercalating into the graphite. By adjusting the number of intercalated fluorine atoms, the properties of fluorocarbon can be altered without showing a significant change in volume [15]. However, even using an organic solvent, another issue prevented the application of Li metal as the anode electrode. During charging and discharging, when Li^+ ions go back from the layered anode to Li metal, dendrites are formed upon crystallization and start to penetrate the separator, causing a detrimental short between cathode and anode [16].

For this reason, Whittingham started his research about finding other materials that can be intercalated by other elements, for both anode and cathode. TiS_2 showed the ability to react reversibly with Li^+ by accommodating lithium ions between every two layers [17]. Since secondary batteries are based on the directional movement of electrons and ions, in this way transferred electrons and ions can be stored in the electrodes without causing much volume change since they are essentially being intercalated. Evidence supported that this kind of Intercalation Compound (IC) are ideal candidates for lithium-ion battery anodes, due to their high volumetric stability and high conductivity. Besides, via the reversible reaction of element intercalation and de-intercalation, the secondary battery can be realized. This idea was also applied on anode material, and by intercalating and de-intercalating lithium ions on both electrodes, electrodes themselves are not directly involved in the reaction, hence very little volume change is seen. Technically, this is the start of the secondary lithium-ion battery.

After this, batteries based on intercalation had attracted much attention, and this technology matured fair quickly. Li et al published that by using $LiCoO_2$ as the cathode, the cathodic potential

is high, which leads to a high voltage in the battery [18], Akira Yoshino [19] also published that graphite is an ideal anode candidate, due its abundancy, low price and stable properties, it has very quickly become the most ideal choice for anodes in the commercialized lithium-ion battery.

It did not take very long before people became unsatisfied with its capacity and started to search for other potential anode materials. Many different lithium metal alloys were investigated since the year 2000: $Li_{13}Sn_5$ [20], Li_9Al_4 [21], $Li_{15}Si_4$ [22] to name a few. The latter is especially attractive not only because of its extremely high specific capacity at a theoretical value of 4200 mAh/g [23], but also because of its abundance and low price. The most prominent issue that comes with the Si anode is the high volume-expansion rate at over 300% during charging and discharging (phase transformation from Si to $Li_{15}Si_4$), which ultimately leads to battery failure. Since atoms in crystalline silicon are densely packed, researchers have put much effort into making the structure of Si more porous [23], and use nano-structuring technology, to make the silicon more expansion-proof. This development is still on-going.

With this in mind, we dive a little deeper into the two materials of interests: carbon-based material and silicon-based material.

1.3.2 Carbon-based material as lithium-ion battery anode

Carbon-based materials have been comprehensively studied since lithium batteries were invented at the end of the 1980s and early 1990s [24] and they remain one of the most focused and commercially successful classes of materials. There is a broad range of structures regarding carbon anodes as can be seen from Figure 4, including carbon nanotubes, carbon-based composite material, graphite, coating of the polymer, and other forms of carbon, etc.

Figure 4. Carbon-based material with different structures as the anode in Li-ion batteries, carbon nano-tube (left), fullerene (middle), and layered graphite (right) [25].

The most attractive character of carbon nanotube (CNT) is that lithium ions can reside on both the inner and outer surface and thus the capacity can thus be significantly increased. Multiwall carbon nanotubes (MWNTs) are multi-layered carbon nanosheets rolled into the shape of a tube. They can be produced by de-composited hydrocarbons such as acetylene [26] with the aid of a catalyst or using electric arc technique [27]. As can be imagined, electrochemical properties of MWNT anodes depend much on the structures of wall layers. Due to the lack of structure, there will be more micropores, voids sites and surface area for lithium ions to occupy in the amorphous, or less graphitic MWNT anodes, thus it shows a higher capacity than well-structured ones (640 mAh/g compare to 282mAh/g) [28].

The biggest problem with MWNT anodes is the unacceptably high irreversibility due to the detrimental reaction occurs on electrode surfaces with ions or particles in electrolytes [29][30]. To deal with this, there have been attempts trying to isolate the carbon material from the electrolytes by burying the carbon inside a matrix, forming composites. Metals such as tin themselves can be lithium active and accommodate Li^+, forming $Li_{22}Sn_5$ [31]. However, with this material stress was introduced by expansion/contraction during lithiation (Li^+ ions inserted into Sn) and de-lithiation (Li^+ extracted out from Sn) process can cause the pulverization of tin anodes, leading to low recyclability [32]. Thus, Sn in itself is not a good anode material, but can a good candidate to protect the MWNT. By combining carbon and metals into composites, a high reverse capacity can be achieved and values in the 40th cycle at a 0.1 C rate of 844 mAh/g have been reported, corresponding to a capacity retention ability of 93.8% [33].

Graphite has been long used for as anode material for lithium-ion batteries, based on the mechanism of lithium intercalation and deintercalation. It has been shown to have a high capacity (372 mAh/g with a stoichiometry of LiC_6) [34], a low operating potential, and an affordable price. The volume expansion of graphite upon charging and discharging is very small, at almost zero.

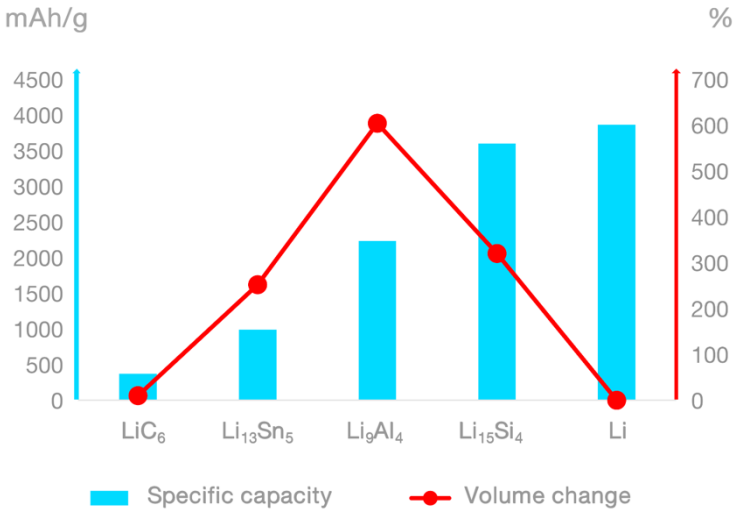

Figure 5. Comparison of the specific capacity (mAh/g) and volume expansion rate for different anode material for Li-ion batterie [35].

Ethylene carbonate (EC) and propylene carbonate (PC) are the two most widely used electrolytes for graphite anodes. Although it is a huge commercial success, propylene carbonate (PC) based electrolyte has a major flaw, as graphite can dissolve in it, resulting in graphite exfoliation. On the other hand, EC electrolyte has a much higher melting point (39 °C), which means that it does not function as well as PC electrolytes at low temperature [36]. To cope with this issue, Masaki Yoshio et al. reported a method of coating natural graphite with a carbon coating. In this paper, natural graphite was treated at 1000 °C and was coated via the thermal vapor deposition method [36].

1.3.3 Silicon-based material as lithium-ion battery anode

Silicon, due to its exceptionally high specific capacity, has attracted lots of attention to be used as the anode in lithium-ion batteries. However, also its high volume-expansion (at around 300%, see from Figure 5) during lithiation can lead to anode pulverization and continuous side reactions, preventing it from being commercialized. The reason behind such significant volume expansion is that the reaction between Li^+ ions and Si involves phase transformation

$$Si + 4.4Li^+ + 4.4e^- \leftrightarrow SiLi_{4.4} \qquad \text{Equation 5}$$

Theoretically, each Si atom can store up to 4.4 Li^+ ions, however, this number tends to be 3.75. The lattice constant of lithium silicide ($SiLi_{3.75}$) is significantly larger than of pure Si (10.6852 Å [37] compared to 1.92 Å [38] at room temperature). For crystalline Si, solid-state amorphization will happen and leads to a less densely packed structure of Si atoms. This volume expansion is detrimental for the battery performance for 2 reasons.

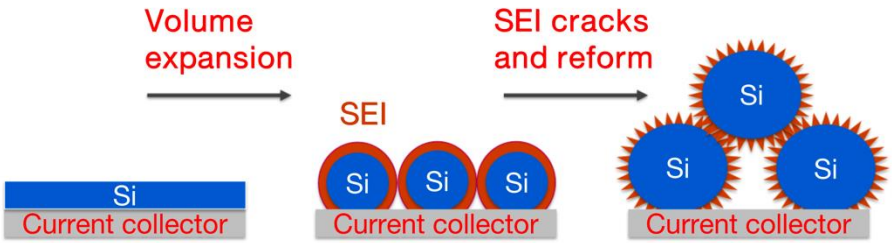

Figure 6. Schematic illustration of the failure mechanism of Si electrode due to Si atoms expansion in Li-ion batteries.

1. As can be seen from Figure 6, a thin-film Si anode is originally attached to the current collector, which is usually a conductive metal foil such as copper and aluminum used to collect current. When the Si anode expands upon lithiation, it will swell and detach from the current collector thereby causing battery failure.
2. As explained in Section 1.2, the SEI layer formed during the first charging cycle will crack due to the expansion and exposes more Si again to the electrolyte, continuing to form SEI layers and continuing to consume Li^+, resulting in a quick capacity fade.

Binders in Si-based anode

To prevent pulverization of Si from on the current collector, binders can be used to interconnect Si atoms. At first, a wide range of polymers is used as binder materials, until in 2003 Chen et al. demonstrated that the cycling performance of amorphous silicon alloy particles could be improved by replacing the traditional binder poly(vinylidene fluoride–tetra-fluoroethylene–propylene) (PVDF–TFE–P) [39]. Sodium carboxymethyl cellulose (NaCMC) was also studied. It was shown that with this binder a much higher performance could be achieved than with traditionally used PVDF, maintaining a capacity of 1200 mAh/g at a rate of C/28 after 70 cycles [40]. A binder should have three specific qualities: (i) the binder should have a weak interaction with the

electrolyte; (ii) in the meantime it should provide paths for lithium ions to get in and move to the silicon anode; and (iii) the binder should have the ability to form a deformable and stable SEI layer. NaCMC has all three qualities, thus making it an excellent binder. The mean issue is that the binder in itself adds much weight to the anode, so decreasing the specific capacity. Furthermore, polymer binders are not always stable and sometimes react with Si, resulting in products that can clog the path for Li^+ ions diffusion [41].

Porous Si particles as lithium-ion battery anode

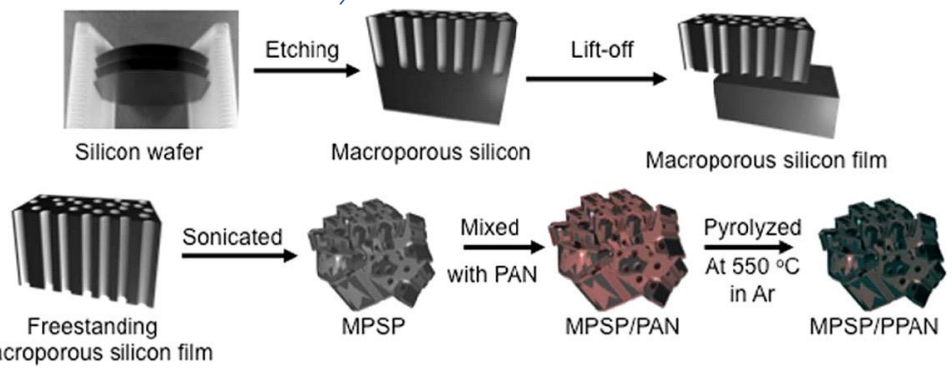

Figure 7. Description of the process to generate a Macroporous Silicon particulate (MPSP)/pyrolyzed polyacrylonitrile (PPAN) composite material from a freestanding macroporous silicon film [42].

Besides using binders, other properties can be modified regarding the structure of silicon itself. The use of silicon nano-particles is one of the most commonly adopted technique. There are mainly two applications. One is to make porous silicon, the other is to make silicon particles as the core, then covered with a mechanically flexible material such as graphite. The manufacturing method of microporous silicon particles for lithium-ion battery anodes has matured around 2007 and 2008, mainly using a microporous silica reduction process [40]. Anodes made by this method offers a performance of 3052 mAh/g initial specific capacity, and 1095 mAh/g capacity was remained after 48 cycles at a current rate of 2000 mA/g, corresponding to a 35.9% capacity retention [43]. The mechanism behind such high performance is based on the porous structure. The pores and voids inside the particles act like a buffer for volume expansion and contraction. Another reason is that the local current density is lowered by the porous structure, which leads to a lower concentration gradient of lithium ions. This lowers the inner stress produced in the first place.

As is shown in Figure 7, porous silicon nanoparticles can be made from etching silicon wafer using HF, then the freestanding porous silicon after liftoff can also be converted into a particulate structure and combined with polyacrylonitrile（PAN) or any binder to form a slurry, thus adapting itself to a roll-to-roll process for mass production.

Si core-shell structure

Another idea besides porous silicon particles is the hollow silicon shell or core-shell structured composites. The hollow silicon shell is manufactured by chemical vapor deposition (CVD) method,

depositing Si on silica layers, followed by a series of reduction and etching process, The resulting structure is a series of interconnected spheres as is shown in Figure 8 [44]. To start with, by adopting this structure the inner stress generated is lower than when using solid spheres. Besides, the hollow structure provides accommodation for volume expansion during the charging and discharging process. Another advantage of this structure is that because all spheres are connected there will be no need for binders. It is reported by Yao et al. they have achieved a high initial discharge capacity of 2725 mAh/g with less than 8% capacity degradation every hundred cycles for 700 total cycles.

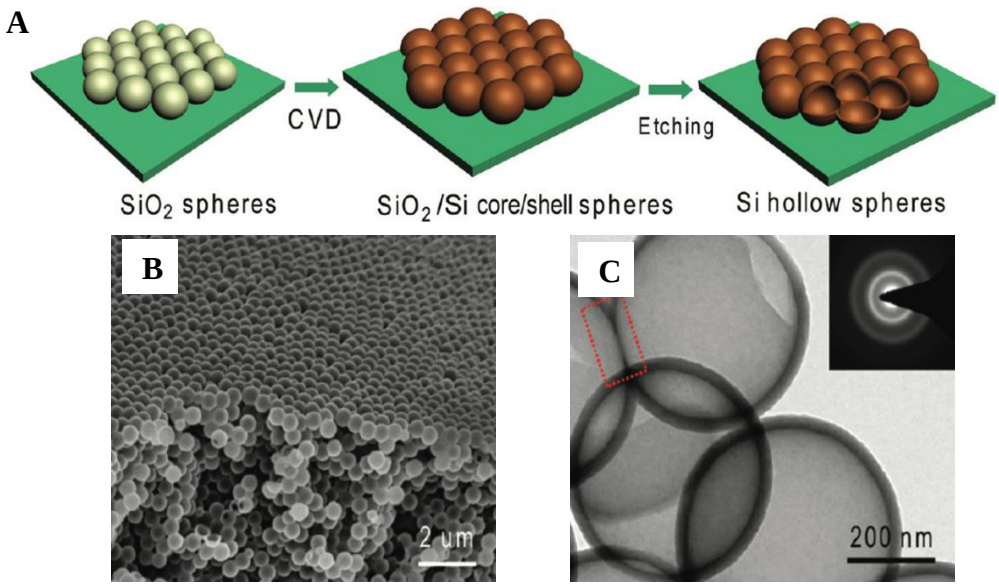

Figure 8. (A) schematic illustration of the manufacturing of Si hollow shell. (B) SEM cross-section view of Si hollow shell structure. (C) SEM demonstration of interconnected structure between Si hollow holes [44].

As can be seen from Figure 8 (A) [44], a template approach was adapted to manufacture the hollow Si structure. First, colloidal silica particles with a diameter of 350 nm are prepared, which are then coated by a stainless-steel layer with 10-20 mm thickness. In the next step, CVD is used to deposit an amorphous Si layer on the stainless coating, after which the silica cores are removed by dilute HF etching. Figure 8 (B) shows a cross-sectional view of the resulting structure while Figure 8 (C) demonstrated the connection between each particle [44] The stainless steel current collector can also be coated by other materials, such as carbon coating [45], and Ti coating [46]. In fact, besides the mentioned application of Si, other means of nano-structuring including Si nano-tubes and Si thin films, all provide a promising direction to lithium-ion battery application. These methods share more similarities than differences, with the general idea to create more space to accommodate the volume expansion upon lithiation.

1.4 Amorphous SiC as the anode material in lithium-ion battery

1.4.1 Structure of a-SiC$_x$:H

One of the most characteristic features of silicon carbide (SiC) is that it exhibits polymorphism, which means it can be present in different structures, named polymorphs. Until 2006, there are known more than 250 types of polymorphs in SiC, each with unique structures and lattice constant [47].

The structure of hydrogenated amorphous silicon carbide (a-SiC$_x$:H) is more dynamic and flexible than its crystalline counterpart. For example, it can be shown by FTIR and Raman Scattering (RS) that there is no Si-Si bond anymore in carbon-rich a-SiC$_x$:H, and carbon tend to cluster at higher carbon concentration [48]. As can be seen from Figure 9 (figure drawn based on [49]), -CH_3 and H can be observed.

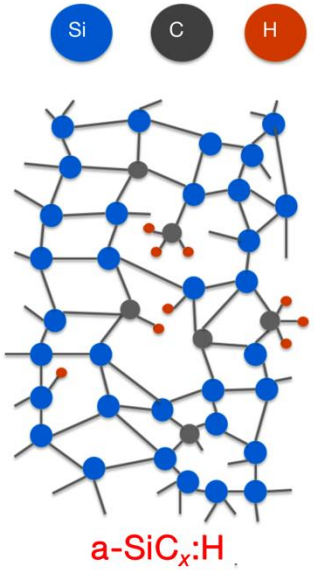

Figure 9. Schematic illustration of the structure of a-SiC$_x$:H.

1.4.2 Synthesis of a-SiC$_x$:H

SiC exhibits many excellent electrical and mechanical properties, and was applied in many fields such as semiconductors, automotive, high resistant coatings and was used as a reflective layer in solar cells [50]. SiC is in itself rare in nature. In 1824, Berzelius reported for the first time the synthesis method for material containing Si-C bonds, and this is a start of the volume production of SiC for industrial uses [51]. Of course, the purity of SiC made from this method was rather low. Relatively pure SiC was synthesized by Lely in 1955 using sublimation technique [52]. This technique undoubtedly accelerated the development of the SiC synthesis in the semiconductor industry in the late 1960s, and for the first time Shockley pointed out the promises of SiC in high-temperature applications [53]. The Lely method was improved by Tairov and Tsvetkov in the late 1970s for the reproducible production of SiC growth [54]. It was not until the 1980s that the liquid

phase epitaxy (LPE) growth of 6H-SiC was invented, as an even further improvement of the Lely method [55]. CVD method was then invented a while later as a method of fabricating high-quality 6H-SiC as well as a-SiC$_x$:H [56].

The synthesis SiC thin film is a different story than that of the bulk SiC. Thin films, if of crystalline structure, should be synthesized in a way that the crystal orientation, defects density, lattice parameter can be controlled. On the other hand, for amorphous SiC thin films, porosity, composition and the percentage of different types of polymorphs present should also be controlled during the synthesis. For both cases, the thickness, stress generated and the doping of the prepared thin films are of importance. Ways commonly used in making amorphous SiC thin films can be generally categorized into Physical Vapor Deposition (PVD), Chemical Vapor Deposition, and Chemical Etching.

1.4.3 Anode application of a-SiC$_x$:H

It can be seen from the previous analysis that both silicon and carbon have their strong sides and deficiencies for application as the anode in Li-ion batteries. Carbon anodes are stable and safe, hence can be easily commercialized, however, with a less than satisfying specific density. For silicon anodes the properties almost the other way around, with an ultra-high specific density, yet a low life expectancy due to the volume expansion during lithiation and de-lithiation process. It intuitively makes sense that by alloying the two materials we end up with something somewhere in between, a combination of properties from both materials. That leads us to the idea of using a-SiC as the anode material.

The theoretical support is as follows:

1. By introducing C in Si, Si concentration can be diluted and the volume expansion of the whole anode can be alleviated.
2. The amorphous structure of a-SiC$_x$:H provides many micro and macro pores that can accommodate the volume expansion.
3. The reaction between a-SiC$_x$:H and Li^+ ions take two steps.

$$SiC + Li^+ + e^- \longrightarrow Si + LiC \qquad \text{Equation 6}$$

$$Si + 4.4Li^+ + 4.4e^- \leftrightarrow SiLi_{4.4} \qquad \text{Equation 7}$$

The first reaction is irreversible and forms pure Si and LiC. Si will further react with Li^+ reversibly just like a normal Si anode, while LiC, which is a ductile material, will stay in the system and serve as a matrix to buffer the expansion [57]. Lastly, a-SiC$_x$:H has a much higher thermal stability compared to pure Si, indicating a better performance under high temperature.

As a matter of fact, unlike silicon oxide and silicon nitride [58], SiC has always been considered as a lithium inactive material. In the past, researchers have been trying to avoid the formation of SiC, because it was considered to be an inactive anode material. This was hard to avoid due to the strong bonding tendency between Si and C [22]. However, recently, it has been confirmed both theoretically and experimentally that a-SiC is a viable solution for anodes. Very lately, in the year 2018, Huang et al. [22] demonstrated this. In their paper, they used inductively-coupled-plasma chemical-vapor-deposition (ICP-CVD) to fabricate a 500-nm thick a-SiC_x:H film, which due to the low synthesis temperature (350 °C) shows an amorphous structure as confirmed by XRD. They also showed that the capacity and recyclability of the battery is closely related to the film thickness. Using 250-nm thick a-SiC_x:H samples they achieved an initial specific capacity of 917 mAh/g, degrading gradually to 376 mAh/g after 100 cycles. This corresponds to a capacity retention of 41%, which is indeed better than for pure Si anodes.

1.5 Objective of the project

It can be seen that the reason why a-SiC_x:H is a potential good anode material is due to the existence of carbon and pores, hence those are two parameters of interests. In the work of Huang et al. [22] they only used stoichiometric SiC (so with $x = 1$) for battery tests and only confirmed its functionality without investigating how the carbon concentration and porosity influence the battery performance.

The main objective of this project is to study the electrochemical performance of a-SiC_x:H as the anode material in a lithium-ion battery, more specifically the performance regarding specific capacity and the ability of capacity retention, and how those performances are influenced by the carbon concentration and porosity.

2.Experimental procedures

2.1 Sample preparation

2.1.1 Plasma Enhanced Chemical Vapor Deposition (PECVD)

Working principle of PECVD

Chemical vapor deposition (CVD) is a commonly used technique in thin-film manufacturing, transforming the gaseous phase to the solid phase. In this process, volatile precursor gases react on the heated substrates and form thin films. In Plasma Enhanced CVD (PECVD), the energy required for the reactions comes from the plasma that is created by RF electromagnetic waves, instead of from heat. In this way, substrates can be kept at a lower temperature, which favors the amorphous structure of a-SiC_x:H.

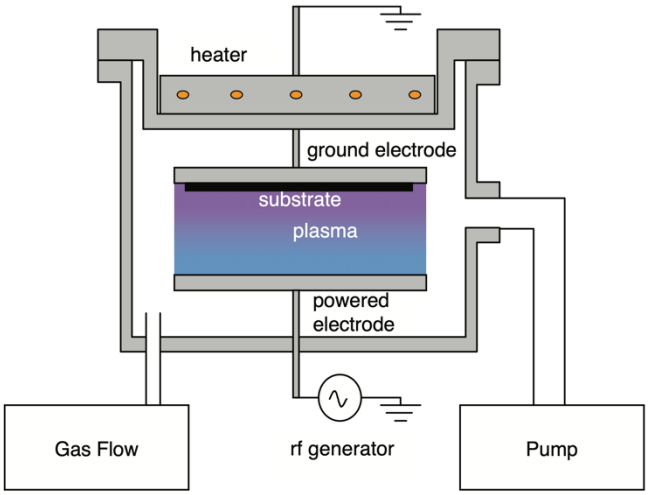

Figure 10 Schematic of a capacitively-coupled RF-PECVD reaction chamber [52].

In this work, all a-SiC_x:H samples were deposited by Plasma-Enhanced Chemical Vapor Deposition (PECVD) in DPC (deposition chamber) 2 and DPC 4 of AMOR multi-chamber system in Cleanroom 10000 of the Else Kooi Laboratory (EKL).

Figure 10 [52] is a schematic illustration of the PECVD equipment used. Substrates were cleaned and placed on a metal holder. Together they were placed inside the deposition chamber and were connected to the ground electrode, the powered electrode is beneath the ground electrode in parallel. Source gases are injected into the chamber from the bottom left and exhaust gases are pumped out from the bottom right after the reaction. A throttle valve is used to control the pressure in the deposition chamber during processing

When source gases are injected into the chamber and the pressure has stabilized, a spark ignites the gases into a plasma that consists of a complex mixture of ions, radicals, atoms, and electrons.

These plasma products then react on the surface of the substrates, and the growth of the film starts.

AMOR PECVD reaction set up

There are in total 5 deposition chambers on the AMOR deposition system, of which chamber 1-4 are for a specific deposition type (n-type, p-type, intrinsic, novel materials), and chamber 5 is a flipping chamber. Specifications of the equipment can be seen in Table 1.

Table 1. Technical specification of the PECVD used.

Machine specifications	Values
Chamber used	DPC 2 and 4
Electrode distance	21 mm
Electrode type	Showerhead
Electrode size	12 cm^2
Electrode area	144 cm^2

Deposition strategy and conditions

A serious of deposition was conducted under different RF power *P* and methane flow fraction, R = $\phi(CH_4)/ [\phi (CH_4) + \phi (SiH_4)]$, where $\phi (CH_4)$ and $\phi (SiH_4)$ is the flow rate of methane and silane respectively, both in standard cubic centimeter per minute (sccm). In total, 30 samples were synthesized by varying the power between 3W, 6W, 9W, 12W and 15W, and varying the methane flow fraction in different values of R = 0, 0.1, 0.3, 0.5, 0.7, 0.9, as can be seen in Table 2.

Table 2. PECVD deposition of a-SiC_x:H varying power and methane flow fraction.

P \ R	0	0.1	0.3	0.5	0.7	0.9
3W						
6W						
9W						
12W						
15W						

The properties of samples were determined by many factors such as methane flow fraction, deposition power, and other deposition parameters shown in Table 3. By varying the methane flow fraction, R, carbon concentration can be controlled. When all other deposition parameter remains constant, a higher methane flow fraction results in a higher carbon concentration in the sample. Of course, by influencing the carbon concentration, the structure of a-SiC_x:H can also be changed. By varying the deposition power density, *P*, the structure of a-SiC_x:H samples, such as porosity can be effectively changed.

Table 3. Deposition parameters kept constant in this work.

Deposition Parameters	Values
ϕ (CH_4) + ϕ (SiH_4)	40 sccm
ϕ (PH_3)	11 sccm
Chamber pressure	0.7 mbar
Substrates temperature	180 ℃

As can be seen from Table 3, total reactant gases-flow rate and chamber pressure were kept constant, to ensure different depositions can be compared and the gas residence time is the same. PH_3 (2% diluted in H_2) was used to make the sample n-type doped, this was to increase the electrical conductivity of the anode and at the same time, the capacity retention ability can also be improved to some extent by n-type doping, comparing to p-type Si and undoped [59]. Due to the low reaction temperature of PECVD, substrates can be kept at a temperature of 180 ℃, which favors the formation of the amorphous structure.

2.1.2 Metal evaporator

Working principle of the metal evaporator

Metal evaporators are based on Physical Vapor Deposition (PVD). There are mainly 2 types of metal evaporating systems that can be used for metal thin film deposition, E-beam evaporation and thermal evaporation. As can be seen in Figure 11 [60], in the E-beam evaporation system, the targeted metal is bombarded by electrons that are accelerated by a charged tungsten filament and ed into the gaseous phase. Those atoms then precipitate again into solid form, coating everything inside the vacuum chamber with a thin metal film. Thermal evaporation is simpler compared to E-beam evaporation, as in this case heat is applied under the crucible where target metal is contained, causing a rise in vapor pressure inside the chamber. Because the chamber is vacuum, a little increase in metal vapor pressure will lead to the vapor traversing through the chamber and hit the substrates, forming films.

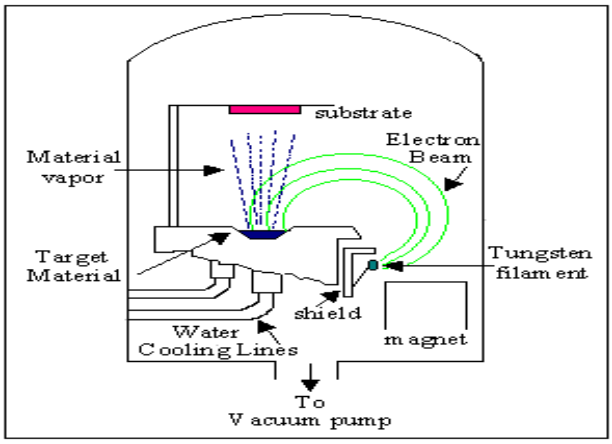

Figure 11. Schematic illustration of the working principle of E-beam physical vapor deposition (EBPVD) [60].

Provac PRO500S

In this work, Provac Pro500S (seen in Figure 12, [61]) located in the cleanroom 10000, EKL, was used to deposit a thin layer of Ti on Asahi glass, for synthesizing pouch-cells in the battery tests. This will be explained more in detail in Section 2.1.3.

Both E-beam evaporation and thermal evaporation modes are available on this equipment. Thermal evaporation is more suitable for source metal with lower melting points such as Al and Cu [61]. Al was not chosen because it tends to be unstable under a low potential environment, which is usually the case for the anode [62]. Copper was not an option for the obvious reason that it is deep contamination for semiconductors, even though it is suitable for this work, it might pollute colleagues' work in the cleanroom. In this work, E-beam evaporation was applied to deposit a 100 nm thick Ti layer on Asahi glass, which will be introduced more in detail in Section 2.1.3.

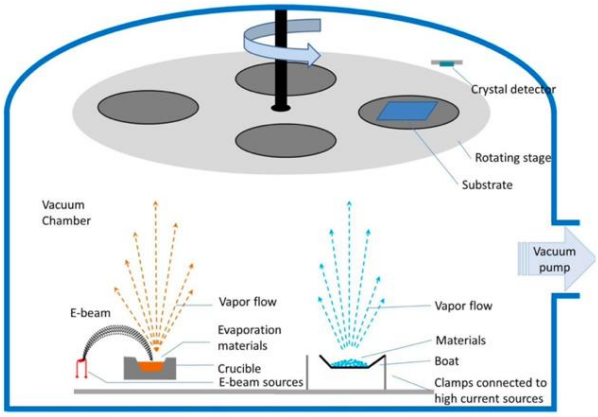

Figure 12. The working principle of the metal evaporator is used to deposit Ti layer [61].

2.1.3 Substrates preparation

In this work, deposited a-SiC_x:H films are very thin, with a thickness of around 1-3 μm. Thus when using PECVD, films have to be deposited on a substrate. Different types of substrates were used for different purposes.

In total, four types of substrates were used: Corning glass and Si wafer are mainly used for material characterization, and Asahi glass substrates and carbon fiber paper (CFP) substrates were used for battery tests a-SiC_x:H films deposited on Asahi glass or CFP can be assembled into pouch cells or coin cells, respectively. Here in this section, glass and Si substrates will be introduced more in detail while Asahi glass substrates and carbon fiber paper (CFP) substrates will be illustrated in Section 2.1.4.

Corning glass-7059

Dimension	0.7 mm thick, size can be shaped as desired
Application	Spectroscopic Ellipsometry (SE) measurements, conductivity measurements, and battery tests
Treatment before deposition	1. A 10 x 10cm substrate was picked up and was ultrasonicated in Acetone and Isopropyl alcohol (IPA) for 10 minutes, respectively. 2. The cleaned substrate was then immersed in 1% Hydrofluoric Acid (HF) for 270 s for a rougher surface to achieve better adhesion of deposited film on substrates.

Si wafer with low doping

Dimension	500 μm thick, 4 inches diameter, 2170-3410 ohm-cm, <100>
Application	SEM/EDS measurements
Treatment before deposition	No treatment was needed, wafers were cleaned already by manufacturer

2.1.4 Battery preparation

Battery tests were performed for chosen samples deposited at the earlier stage of the work, mainly aiming to find out how the battery performances, more precisely, how the specific capacity, initial coulombic efficiency, and capacity retention ability are affected by material properties such as porosity and carbon concentration. It is worth mentioning that in a lithium-ion battery consists of a cathode and an anode and whichever material has a lower potential comparing to Li/Li^+ will be the anode. a-SiC_x:H is referred to as the anode in the previous sections because, in a commercialized battery, the counter electrodes are usually different types of metal oxides, such as Lithium Nickel Cobalt Aluminum Oxide (NCA) or Lithium Cobalt Oxide ($LiCoO_2$) [63]. Those oxides have a potential of around 4 V vs Li/Li^+, while this value for a-SiC_x:H is 0.4 V

[64], which is significantly lower and essentially makes it the anode of the battery. In this work, however, half-cell tests were performed to investigate the properties and performance of the anode material of interests. In a half-cell battery test, the counter electrode is a thin lithium metal foil, which has 0 V potential vs Li/Li^+ and this effectively makes the a-SiC_x:H the cathode. This means just the terminology of anode and cathode are reversed; nothing has changed regarding the electrode reactions and the capacity fade mechanisms of the electrode.

Pouch-cell preparation

Asahi layered substrates for pouch-cell

When using a PECVD chamber of the AMOR deposition system in the cleanroom 10000, one should be careful which material can go inside the deposition chamber. For example, the most commonly used substrates are glass substrates and silicon wafers, in addition, stainless steel substrates are occasionally used. A qualified substrate should at least meet certain requirements, that is, does not decompose under high temperature and vacuum environment, and does not contaminate the deposition chamber with undesired species.

We will now discuss how pouch-cells are made.

Layered structure based on Asahi glass

Dimension	1 mm thick, 2 cm x 10 cm,
Application	To assemble into pouch-cell for electrochemical measurements
Treatment before deposition	1. Asahi glass was picked up and the side with fluorine-doped tin oxide (FTO) coating was determined by a voltmeter, the side with the coating was more conductive while glass virtually non-conductive. 2. Asahi glass was put in Provac (metal evaporator), with the FTO side facing downward, the recipe of '100 nm Ti' was performed. 3. As treated substrates were cut into 2 cm x 3 cm pieces and a-SiC_x:H was deposited onto a 2 cm x 2 cm area, the left 1 cm x 2 cm area was exposed with Ti layer, which was used to connect wires for battery tests.

Asahi glass was purchased from Asahi Glass Co., Ltd. The schematic illustration can be seen from Figure 13, it has a 1 mm thick glass layer, which serves as the mechanical support. On top of the glass is a layer of 700 nm thick Fluorine-doped tin oxide (FTO), this layer was used to increase the adhesion between the metal layer that was going to be deposited next and the glass. Also, the FTO coating is conductive and can help to carry the current. A 100 nm Ti layer deposited by Provac Pro500S mentioned in Section 2.1.2 was used as a current collector, since the conductivity of the deposited a-SiC_x:H film is relatively low.

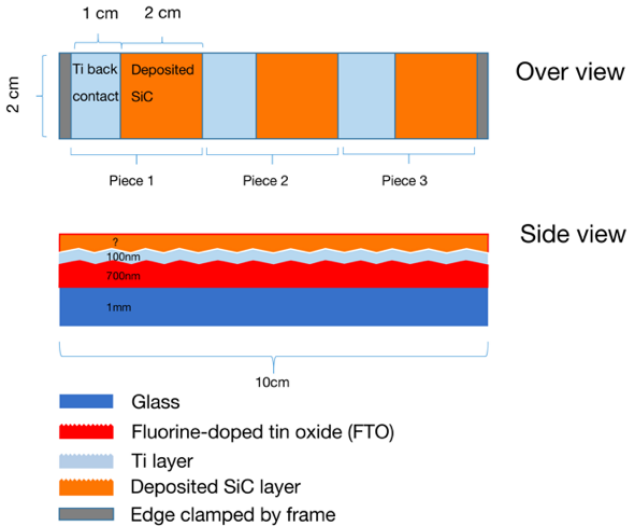

Figure 13. Schematic illustration of the dimensions and structure of Asahi glass-based substrates.

Designed as such, the total thickness of the substrates exceeds 1 mm, to assemble this into a battery pack, pouch cell was the only option.

Pouch-cell assembly

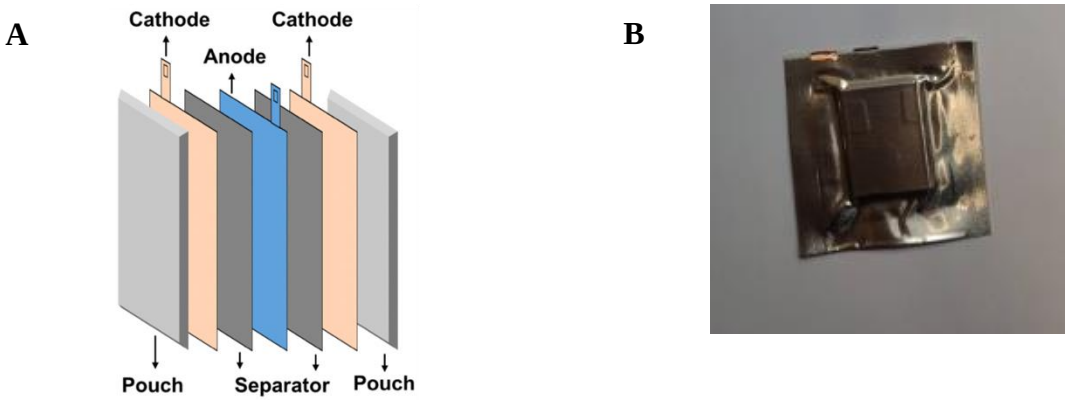

Figure 14. (A) Schematic illustration of the layered structure of pouch-cell [65]. *(B) Assembled pouch-cell by Zhaolong Li for battery tests in this work.*

It can be seen in Figure 14, [65] that in a pouch-cell assembly, multiple layers of the anode, separator, and cathode are stacked on top of each other and are then sealed by a flexible foil. This approach minimizes the dead weight of the battery and improves the energy density of the battery [66]. We performed pouch cell tests on two samples to see if we can get a functional lithium-ion battery system using a-SiC_x:H as the anode.

Coin-cell

A coin cell, also known as button-cell, is a commonly used battery packing technique in laboratory half-cell tests. Coin-cells can be very compact, thus are widely used as the battery in portable devices, the structure of which can be seen in Figure 30 [67]. Carbon fiber paper (CFP) is used as substrates when making coin-cells as this material be cut quite easily into a round shape with a radius of 0.2 cm.

Carbon fiber paper substrates (CFP)

Dimension	Can be cut into the desired size
Application	To assemble into coin-cell for electrochemical measurements
Treatment before deposition	Have to be preserved in a dry environment, no special pre-treatment is needed.

Spectracarb GDL 0550 carbon fiber paper is made of carbon fibers that are connected by resin, as can be seen from Figure 15 [68]. This material is stable up to 400 °C.

In order to avoid cross-contamination, deposition on carbon fiber paper was carried out in DPC4 of the AMOR system, as we did not have information on the possible outgassing under vacuum conditions for this material. The use of this material as the substrates has many advantages:

1. Carbon fiber paper is conductive, there will be no need for an additional layer of metal as the current collector.
2. a-SiC_x:H thin films stick better on carbon fiber paper than on metal, where obvious exfoliation can be observed.
3. Carbon fiber paper is easy to tailor into the desired size and shape and can be assembled in to coin cell conveniently.

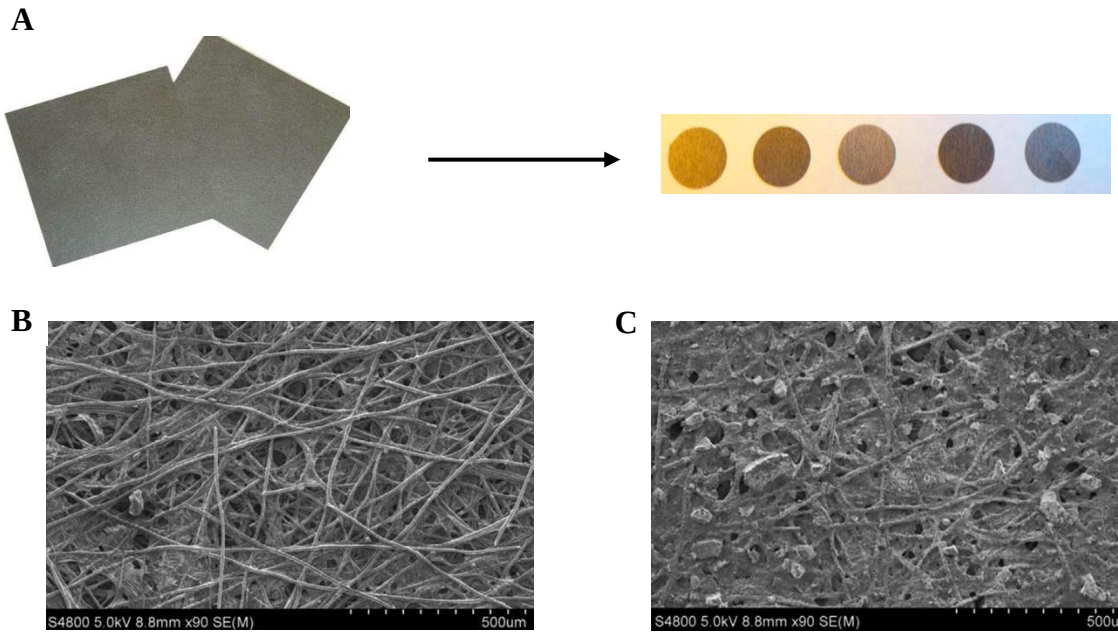

Figure 15. (A) Representation of cutting carbon fiber paper into different shapes, the round shape can be made into coin-cells [69] and (B) SEM images of carbon fiber before deposited with Si/C composites. (C) SEM images of carbon fiber after deposited with Si/C composites [68].

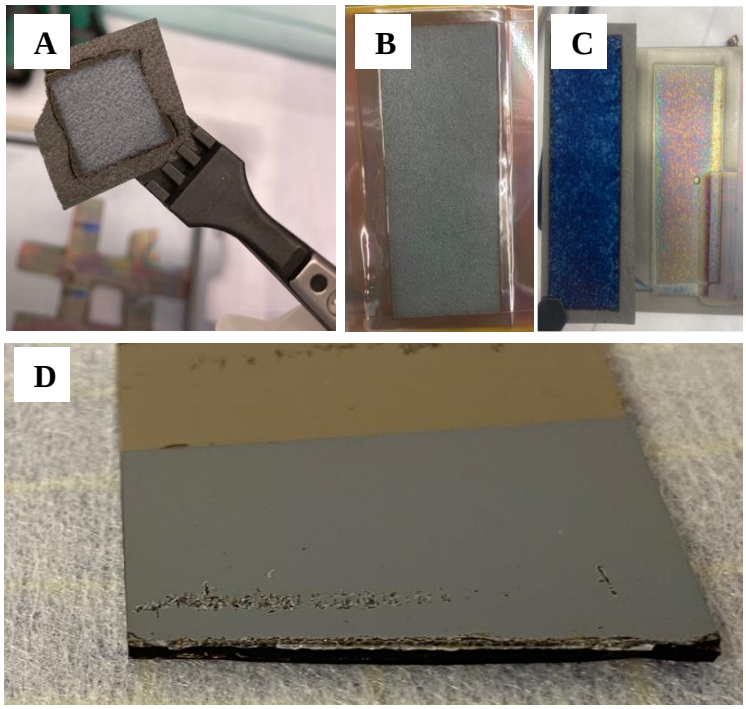

Figure 16. (A) Deposition of a-SiCx:H on carbon fiber paper (B) front side and (C) back side, and (D) a-SiCx:H deposited on layered Asahi substrates

As can be seen from Figure 16 (D), a-SiC_x:H deposited on Asahi layered substrates showed pulverization right after deposition, which is detrimental to the battery performance, the adhesion to carbon fiber paper, on the other hand, is much better, as depicted by Figure 16 (A).

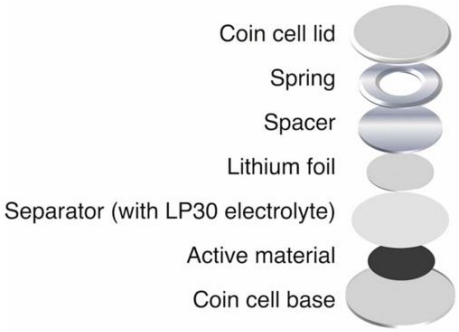

Figure 17. Schematic illustration of the coin-cell half-cell structure [67].

One issue introduced by using carbon fiber paper as the substrates is due to its porous structure, reactant gases can penetrate the layer and reach the metal holder, as can be seen Figure 16 (C). This also causes an issue that deposition rate measured based on deposition on glass substrates should be corrected since not all the material was deposited on substrates when using carbon fiber paper. Tape saw in Figure 16 (B) is the Teflon tape, used to secure the position of CFP substrates. Deposited films can then be assembled into a coin-cell, the schematic illustration of which can be seen in Figure 17.

2.2 Measurement techniques

2.2.1 SEM/EDS measurement

Working principle of SEM/EDS

Scanning Electron Microscopy (SEM) and Energy Dispersive x-ray Spectroscopy (EDS) have been used to characterize the carbon concentration in deposited a-SiC_x:H. SEM has a higher complexity than optical microscopy. It generates a beam that consists of focused, highly energetic electrons, with which information regarding the structure, composition, and morphology of the sample can be obtained by analyzing the interaction between electrons and material [70]. When electrons arrive at the material surface, a fraction of them will have elastic collisions with material particles, (which means the direction of electrons movements were changed but the energy remained the same, most of the electrons interact inelastically). While most electron energy is consumed in producing heat, other interactions will lead to secondary effects, such as backscattered electrons, secondary electrons, characteristic X-ray, etc, as can be seen in Figure 18 (A) Which interaction will dominate is determined by how deep the electrons can penetrate the material, as can be seen from Figure 18 (B).

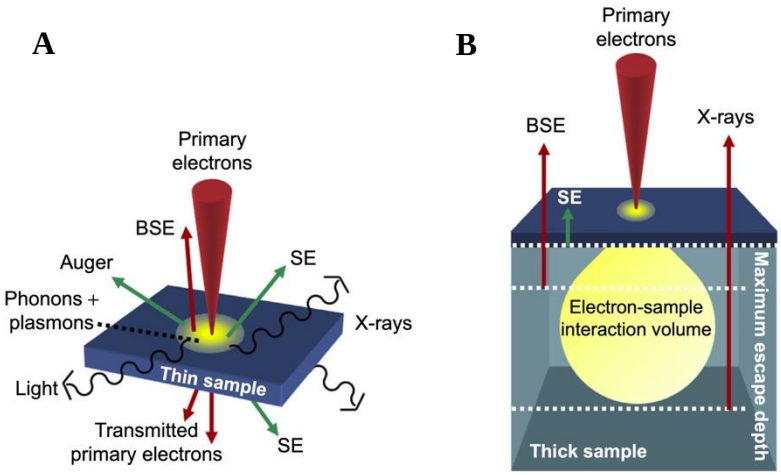

Figure 18. The interaction of incoming primary electrons with a sample. (A) Useful signals generated by electron-matter interactions in a thin sample. (B) Absorption of Secondary electrons (SE), Backscattered electrons (BSE), and X-rays in thick samples, by inelastic scattering within the interaction volume [70].

Among the mentioned secondary effects, the characterized x-ray is the most useful information for material composition analysis. When the accelerated electron beam hits the targeted sample, the electrons from K-shell will be knocked out from the specimen atom, forming a vacancy in that shell. If an electron from another shell fills in that vacancy, the excess energy will be released in the form of high energy photons, which is characterized as x-ray, this process is called electron transition. The generation and energy of the emitting x-ray is highly material dependent, and by analyzing the energy spectrum, qualitative and quantitative analysis of specimen can be performed [71].

Description of SEM/EDS used in this work

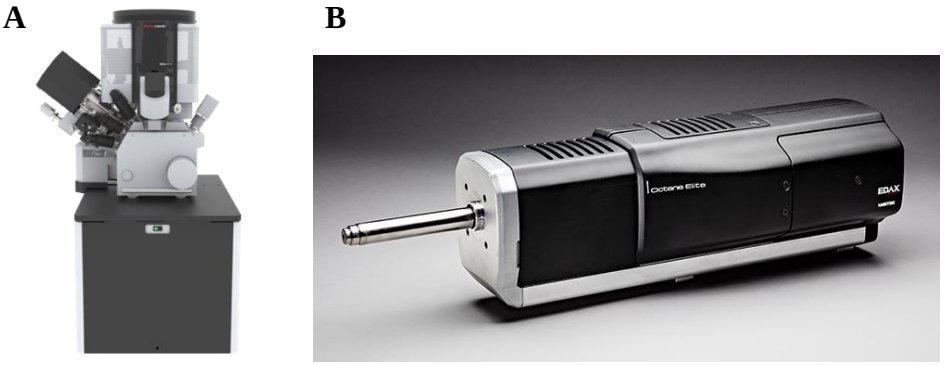

Figure 19. (A) Thermo Fisher® Helios G4 PFIB UXe dual-beam [72]. (B) Ametek ®(EDAX) Octane Plus [73].

In this work, SEM combined with EDS was performed with a Thermo Fisher® Helios G4 PFIB UXe dual beam (see in Figure 19 (A)) [72] combined with an Ametek® (EDAX) Octane Elite Plus (30 mm^2, 125eV) detector (see in Figure 19 (B)) [73] using TEAM™ Pegasus Integrated EDS-EBSD data acquisition suite. The beam energy employed was 5 keV with a beam current of 2.3 nA.

Example of measurement

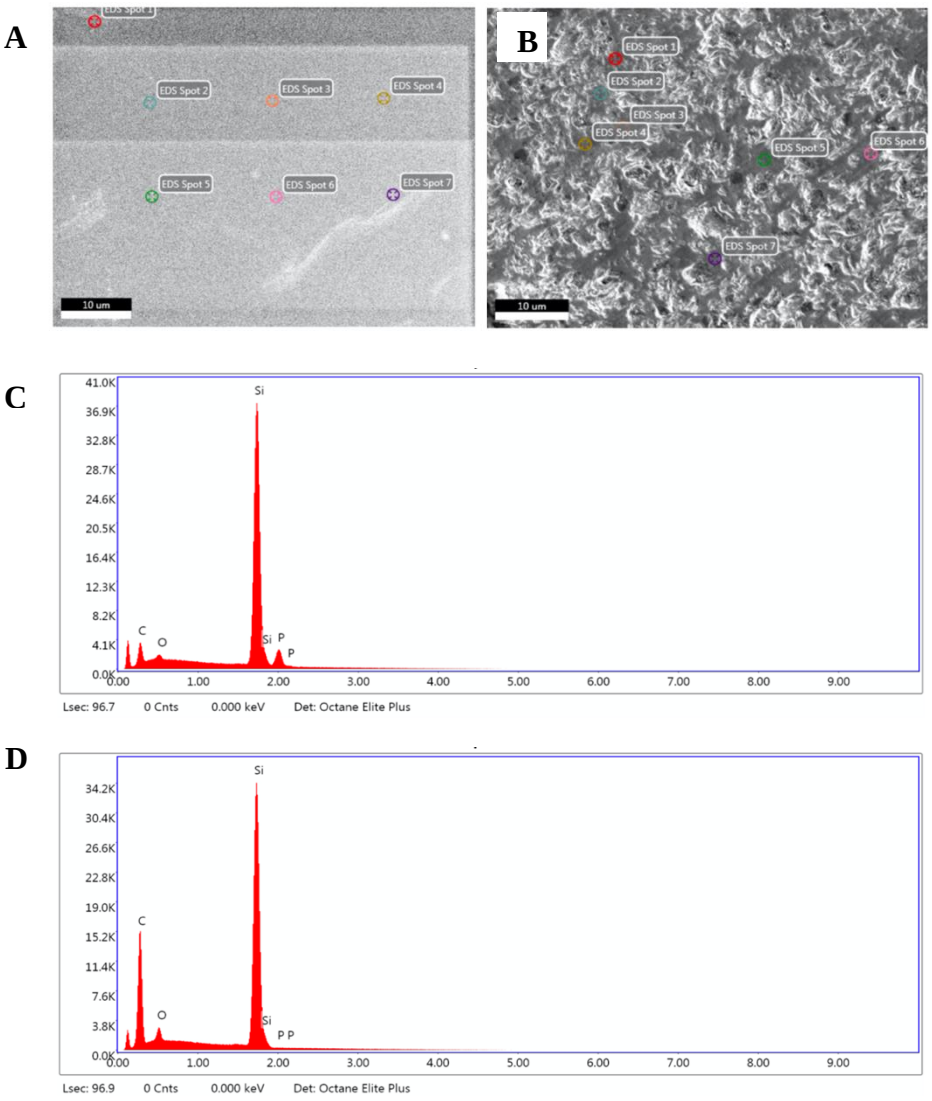

Figure 20 (A) SEM optical image for sample deposited under 3W, R=0.9. (B) SEM optical image for stoichiometric SiC. (C) and (D) are the measurement results for element concentration of sample deposited under 3W, R=0.9 and stoichiometric SiC, respectively.

As can be seen from Figure 20 (A) and (B), 7 points were measured for each sample, then 7 carbon concentration measured and the values were averaged out to calculate the carbon concentration that was most representative for the sample. In Figure 20 (C) and (D) shows typical energy spectra measured by SEM/EDS, with the photon count on the y-axis and the photon energy on the x-axis. The photon energy along the x-axis is element dependent, whereas the photon count along the y-axis reflects the element concentration. The relative element concentration can be acquired by comparing the peak area, which is the integration of the photon number as a function of the energy. The measurement settings were calibrated based on stoichiometric SiC, which has a carbon concentration of around 50%.

2.2.2 Spectroscopic Ellipsometry (SE)

Working principle of spectroscopic ellipsometry

After deposition, each sample deposited on glass substrates was characterized by Spectroscopic Ellipsometry (SE) for thickness, bandgap (Eg), and refractive index (n) at the far-infrared region. Spectroscopic ellipsometry was chosen for the characterization for mainly three reasons:

1. Measurements of SE are quick and generally take less than 30 seconds, this is very beneficial to this research because a large number of samples have to be measured.
2. SE measurements do not require pre-treatment of the sample, nor do they change the integrity of the sample
3. Except for thickness, multiple material properties can be acquired with one measurement, this is effective.

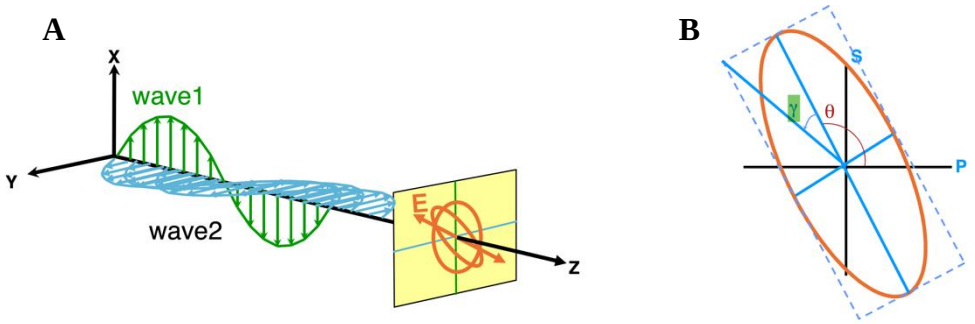

Figure 21. (A) Schematic illustration of the electromagnetic wave before polarization and (B) and after polarization [74].

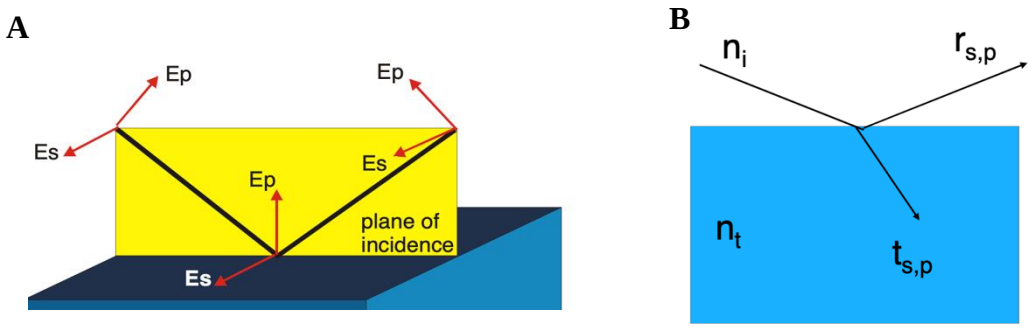

Figure 22. Polarization of light described by Fresnel equations [74]

As can be seen from Figure 21 [74], light is an electromagnetic wave. After interacting with the material, the light will be polarized and will have different intensity in different planes. By measuring the polarization of waves in both S (perpendicular to the plane of incidence) and P (parallel to the plane of incidence) plane, material properties can be obtained. This change in polarization can be expressed in a ratio, which contains two parameters, ψ, and Δ, that can be directly measured by SE.

$\widetilde{r_p}$ and $\widetilde{r_s}$ are the two Fresnel coefficients, that are, two solutions to boundary value problems at material interfaces. As can be seen from Figure 22, they describe the reflection of light at material interfaces in P and S plane, respectively. E_r and E_i are the electric field of the reflected and incident light, respectively.

$$(\widetilde{r_p} = \left(\frac{\widetilde{E_r}}{\widetilde{E_i}}\right)_p = \frac{n_t \cos\theta_i - n_i \cos\theta_t}{n_i \cos\theta_t + n_t \cos\theta_i}) \quad \text{Equation 8}$$

$$(\widetilde{r_s} = \left(\frac{\widetilde{E_r}}{\widetilde{E_i}}\right)_s = \frac{n_i \cos\theta_i - n_t \cos\theta_t}{n_i \cos\theta_t + n_t \cos\theta_i}) \quad \text{Equation 9}$$

$$(\frac{\widetilde{r_p}}{\widetilde{r_s}} = \frac{|E_{out}|/|E_{in}|}{|E_{out}|/|E_{in}|} e^{i(\delta_p - \delta_s)} = \tan(\psi)\, e^{i\Delta} = \rho) \quad \text{Equation 10}$$

As can be seen from equations above, the change in polarization of the light is reflected by two parameters ψ and Δ. In those equations ψ is related to an amplitude ratio and Δ is related to the phase change. These parameters can be measured directly using SE and from these parameters the optical properties of the material can be obtained [74].

Spectroscopic ellipsometry used in this work

In this work, J.A Woollam M2000DI was used, as can be seen from Figure 23. It covers a wavelength range of 193-1690 nm, with 690 wavelengths options, with a data acquisition rate of 0.05 seconds and the maximum thickness can be measured is 18 mm [75].

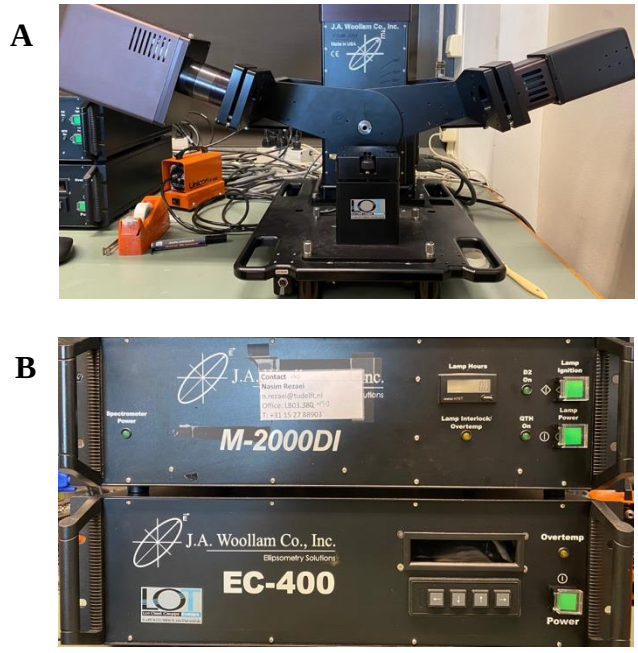

Figure 23. (A) J.A Woollam E2000DI incident device (B) J.A Woollam lamp and power source.

Example of measurements

A

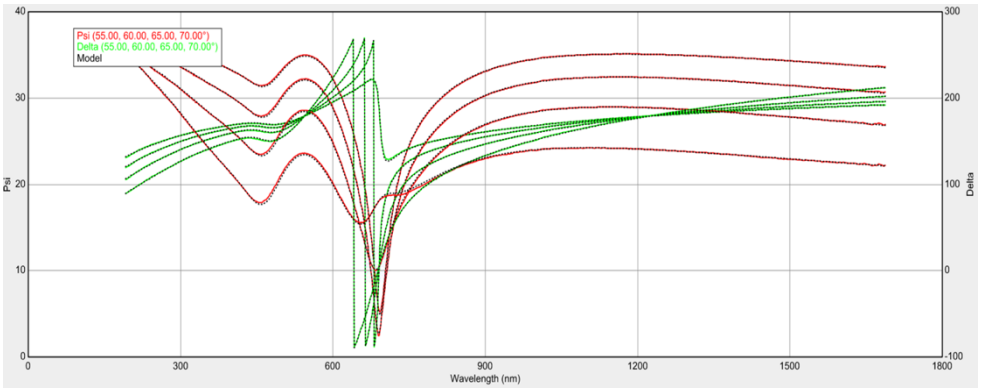

B

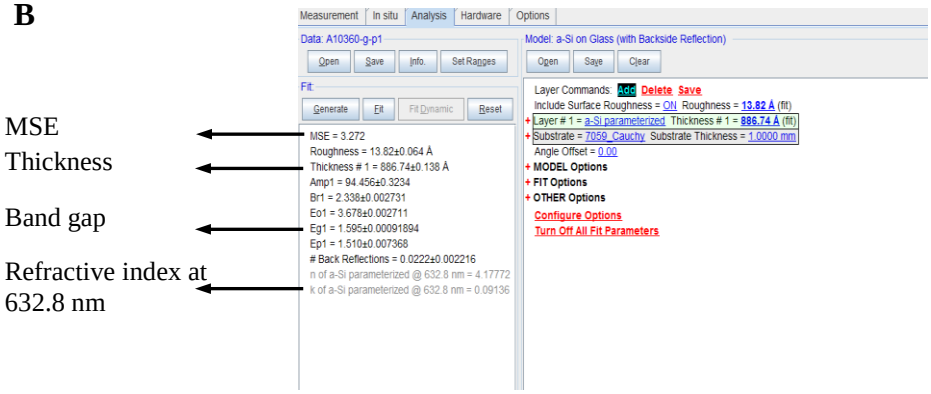

Figure 24. (A) Fitting model of SE and (B) Material properties can be obtained from CompleteEase software for analyzing spectroscopic ellipsometry measurements, and information of samples can be acquired.

Figure 24 shows the data fitting process for the measured sample deposited under 3W and methane flow fraction 0. When the measured data (firm line) does not overlap with the model (dot line), this indicates that the parameters used in this model do not match with the experimental data and in this case and the error will be very large. When measured data overlap with the model (results are considered to be trustworthy when mean-square-error is less than 20, as can be seen from Figure 24 (B)), material properties such as film thickness, bandgap, and refractive index can be acquired. In this case, the fitted thickness for the deposited thin film is 88.67 nm, bandgap 1.595 eV and the refractive index is 4.178, each data is within an error margin. In this measurement the mean square error (MSE) is 3.272, which was very low, indicating the measurement is trustworthy.

Porosity determination based on Bruggeman Effective Medium Approach

Porosity is one of the dominating factors influencing the performance of the anode, thus it is of our interest to determine a value for the porosity. Plenty of research has been carried out regarding porosity detection in thin films. Sophisticated methods such as Brunauer–Emmett–Teller (BET) method and other types of porosimetry connect the pressure of pressing gases/liquid into the material and porosity of the material [76]. In this way, not only the porosity as the volume fraction of voids can be characterized, but also the pore size distribution can be revealed. As the porosity and porosity distribution influences Li^+ ion diffusion and electronic conductivity of the material, it is important to measure these quantities [77].

In this work, due to the limitation of time and a large number of samples, a quick characterization method of porosity was needed that has to provide relatively accurate measurements without involving too detailed information regarding porosity distribution. This can be done by connecting the refractive index of material previously acquired from SE measurements and assumptions on the material structure. The refractive index and density of a material are related. Generally speaking, a higher density comes with a higher refractive index. To investigate the porosity of a-SiC_x:H, Bruggeman's effective medium approach [78] was applied.

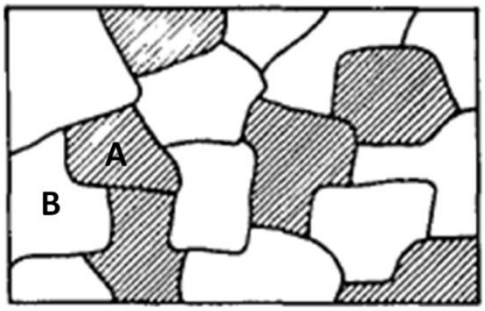

Figure 25. Representation of heterogeneous two-phase media in Bruggeman's effective medium approach, in this case, either phase A or B can be used to represent pores and it makes no difference [78].

Effective medium approximations are theories based on which we can calculate the physical properties of a material based on assumptions on its structural composition. In Bruggeman's effective medium approach, the properties of a mixture consist of two heterogeneously mixed phases can be calculated based on the properties of each component. Specifically for the work presented in this thesis, we assume that for porosity detection in porous material, one constituent is the void and the other one is the bulk material [79]. Bruggeman's effective treats both of the constituents equally without differentiating the host or inclusion (as is shown in Figure 25, pores can be either A or B; the two phases are equally treated, [78]). It can be expressed by the following equation.

$$(1-p)\left(\frac{n_i^2-n_a^2}{n_i^2+2n_a^2}\right)+p\left(\frac{1-n_a^2}{1+2n_a^2}\right)=0 \qquad \text{Equation 11}$$

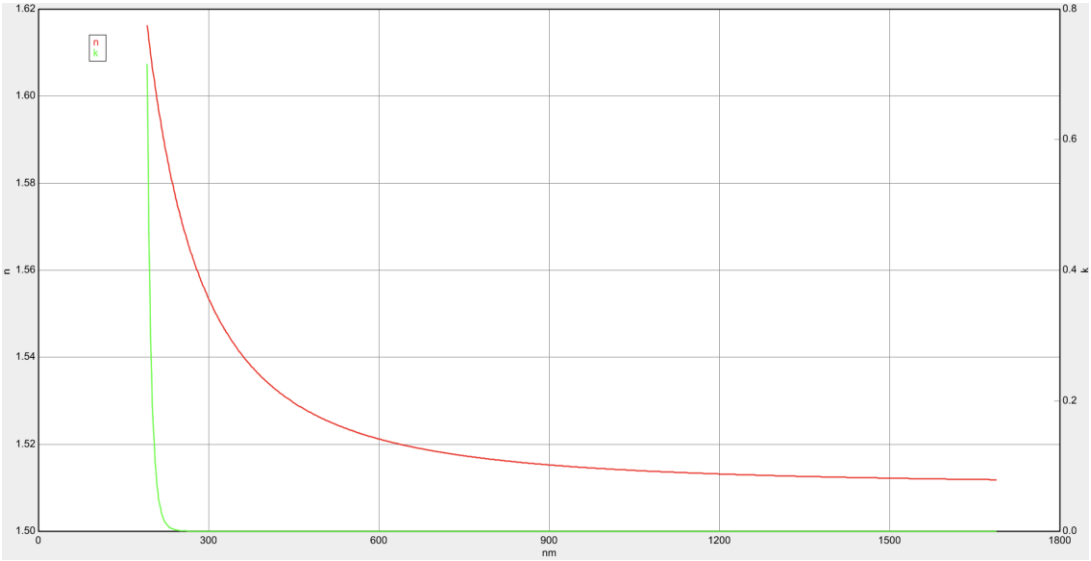

Figure 26. Refractive index in the far-infrared region acquired from spectroscopic ellipsometry.

Where p is the void volume fraction, that is, the porosity, n_a is the measured refractive index in the infrared region of the sample, this can be obtained by fitting SE data as can be seen in Figure 26. n_i is the refractive index of the bulk material with the same composition, but without any porosity [80].

n_i on the other hand, is composition-dependent. This means for bulk materials without porosity, this value will still be different for each deposited sample since they have different carbon concentration. To calculate this composition-dependent value, two extreme values of the refractive indexes for pure Si and C were chosen to be the reference point, by assuming a linear relationship between the permittivity (square of the refractive index) and carbon concentration, $\mathrm{n_i}$ can be calculated. The permittivity of Si was taken to be 12 [81], and that of carbon (carbon black) was taken to be 2.7 [82]. The schematic relationship between permittivity and carbon concentration of each sample can be seen from Figure 27 The permittivity of the stoichiometric SiC was 6.2 [83], indicating a linear relationship can indeed be assumed. Based on the carbon concentration and refractive index at the far-infrared region, the porosity of the sample can be calculated.

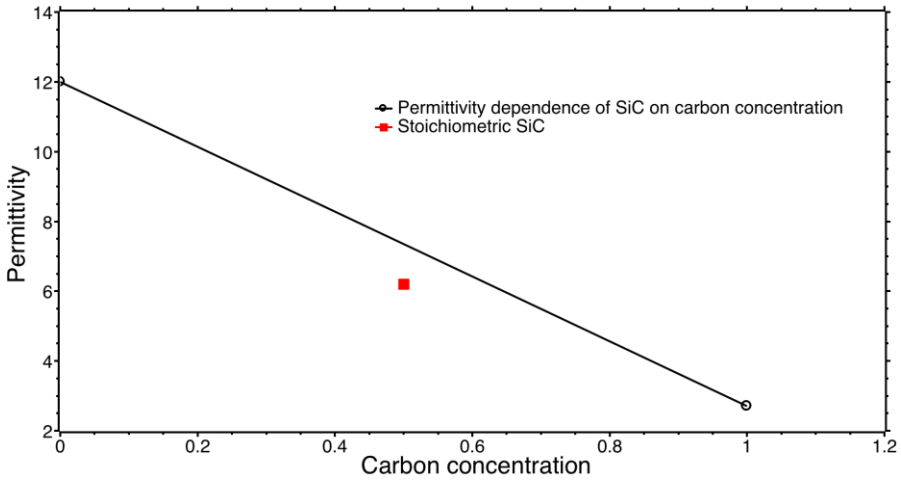

Figure 27. The permittivity of a-SiC$_x$:H as a function of carbon concentration

2.2.3 Electrical conductivity

Working principle of electrical conductivity measurements

The electrical conductivity of deposited a-SiC$_x$:H film was measured using dark conductivity measurement. This is a technique in photovoltaic material characterization and for measuring the activation energy, which reveals information such as the doping level of the sample. The conductivity was measured to evaluate the performance of each sample as the electrode. Meanwhile, this also provides experimental data for COMSOL simulation described in Chapter 5 to investigate the influence of conductivity on the battery performance of a-SiC$_x$:H electrode.

Electrical conductivity describes the level of ease at which charge can pass through the material, this is determined by the density of charge carriers and their mobility, both of which depend on temperature. The conductivity of a-SiC$_x$:H can be expressed in the form

$$\sigma = \sigma_o \, exp(\Delta E_a/kT) \qquad \text{Equation 12}$$

By performing conductivity measurements at temperatures ranging from 60 to 130 ℃ between two coplanar electrodes, it can be derived from the activation energy and extrapolated the conductivity at the room temperature.

Dark measurement set up used in this work

In this work, Keithley 6517B Electrometer/High Resistance Meter was used to measure the conductivity dependence on temperature, as can be seen from Figure 28 (A) [84]. An optical microscope was used （Figure 28 (B)） to connect the contacts with the Al contact layer that was deposited on top of the a-SiC$_x$:H. Samples were annealed before measurements. From the measurements, the resistance of the film can be directly obtained, from which the conductance can be calculated.

A **B**

Figure 28. (A) Keithley 6517B Electrometer/High Resistance Meter. (B) Optical microscope used to connect the contact.

Given the geometrical parameters of the film (in this case, the distance between the two contacts is 0.5 mm and the thickness of the film is 500 nm), the conductivity of the sample can be obtained.

3. Material characterization

3.1 Material properties

3.1.1 Deposition rate as a function of methane flow fraction and deposition power

As was demonstrated in Chapter 2, the thickness of the sample can be obtained by fitting the data measured from samples to a model, using spectroscopic ellipsometry. The thickness of each sample is important to know to calculate the deposition rate (nm/s) under specific deposition settings. Knowing the deposition rate, the thickness of the future deposition can be controlled, this is useful since both SEM/EDS measurements and electrochemical measurements have certain requirements for sample thickness.

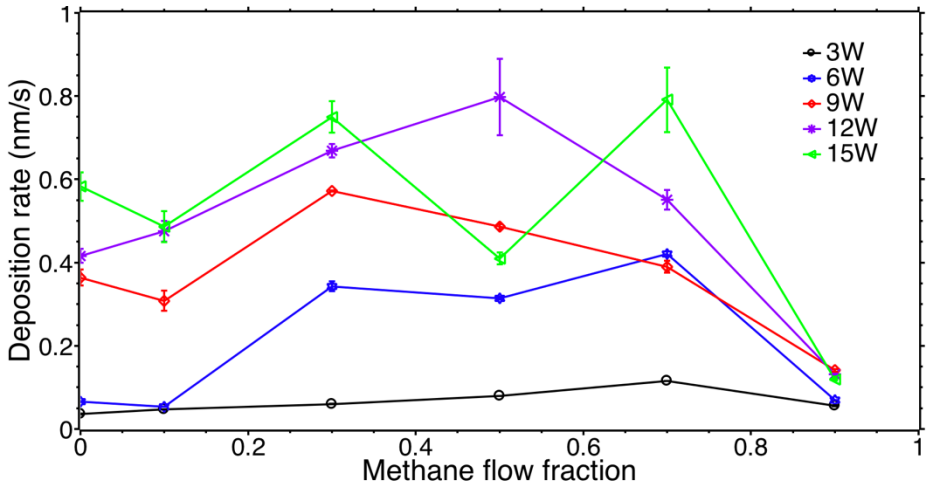

Figure 29. The calculated deposition rate of a-SiC_x:H as a function of methane flow fraction and deposition power.

It can be seen from Figure 29 that the deposition rate increases with a higher deposition power and a higher methane flow fraction. The deposition rate increases more significantly with power in the low power region. This is because in this region, reaction rate depends on the degrees of disassociation of reactant gas molecules [85] and chemical bonds break more thoroughly under a higher deposition power. When the power density increases above a certain level, the power density is no longer the limiting factor for the reaction rate. Instead the transport of radical species becomes the limiting factor, and this is determined by temperature, chamber pressure, etc [85]. Hence, the difference in deposition rate between 12W and 15W is less pronounced than that between 3W, 6W, and 9W. It also shows an increase and decrease of the deposition rate with increasing methane flow fraction. This decrease of deposition rate can be attributed to the higher energy required to break the chemical bonds of CH_4 comparing to that of SiH_4.

3.1.2 Refractive index as a function of methane flow fraction and deposition power

Figure 30 shows the refractive index as a function of methane-flow fraction for different deposition power. It can be seen from this figure that the refractive index decreases with a higher

methane flow fraction and a higher deposition power. Obviously, with a higher methane flow fraction and deposition power the carbon concentration of the sample increases, which leads to a lower refractive index. This can be seen in Figure 31.

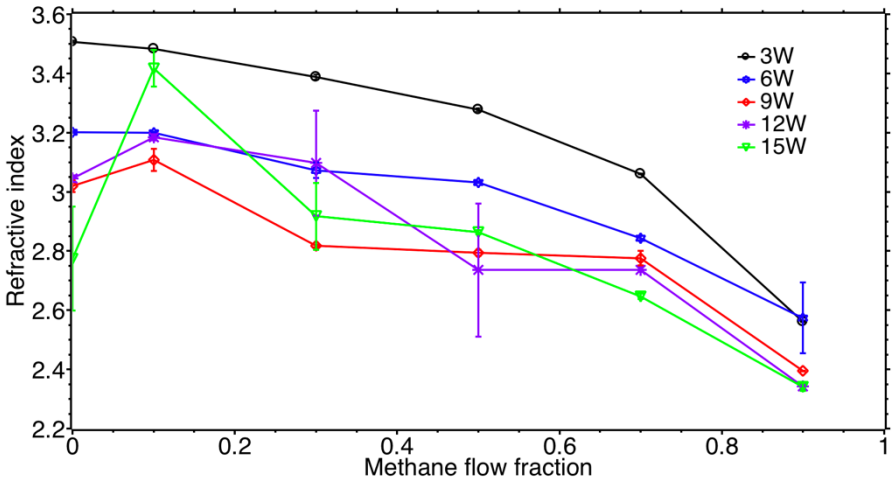

Figure 30. Measured refractive index as a function of methane flow fraction and deposition power.

3.1.3 Carbon concentration as a function of methane flow fraction and deposition power

The carbon concentration of each sample was measured by SEM/EDS. There are requirements for the thickness of the samples, because only when the thickness is beyond a threshold incoming electrons will only interact with the material and not with the substrates. This is important in order to prevent interference due to elements in substrates. The precise requirement for thickness depends on the properties of the material such as density and crystal structure. As a rule of thumb 800 nm is used. It is calculated for crystalline SiC that a thickness of 500 nm is sufficient. However, due to the amorphous structure of a-SiC$_x$:H, electrons can penetrate pores without much energy loss and this needs to be compensated by a higher thickness [86].

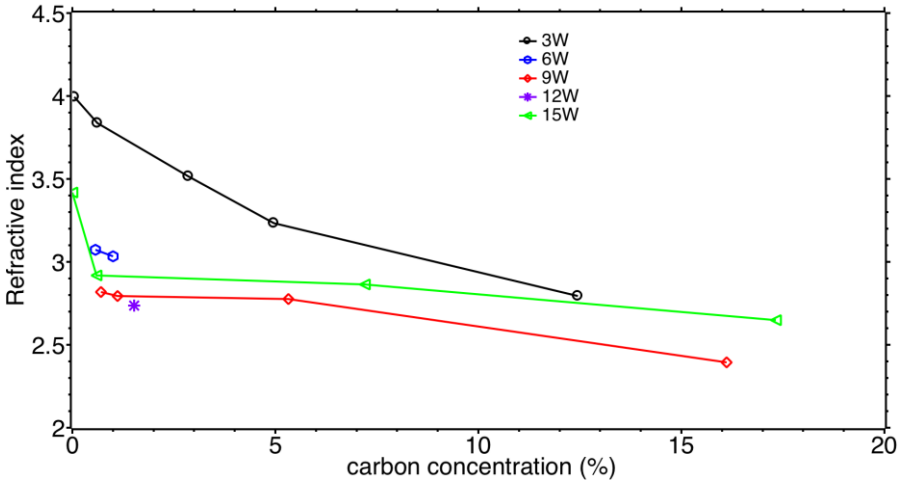

Figure 31. Refractive index as a function of the carbon concentration.

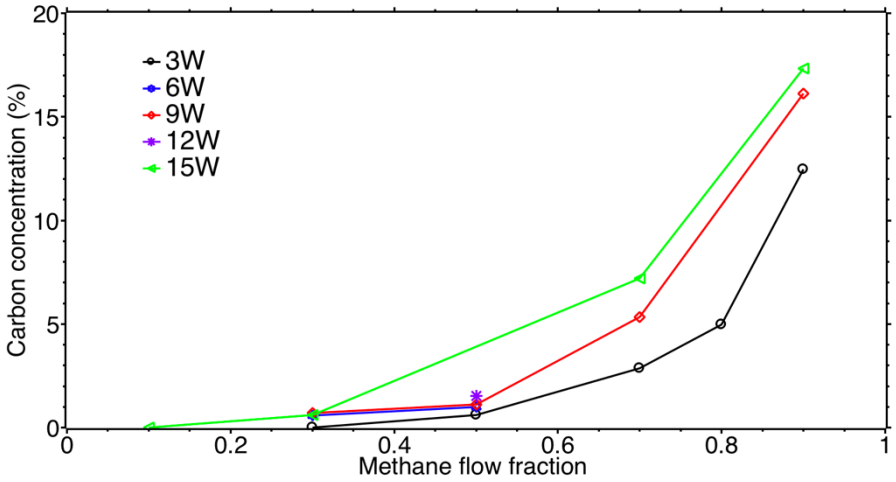

Figure 32. Carbon concentration as a function of deposition power and methane flow fraction.

Table 4. Results of SEM/EDS measurements for element concentration of a-SiC$_x$:H sample deposited under 3W, R=0.9.

Element	Weight %	Atomic %	Net Int.	Error %	Kratio	Z	A	F
C K	5.69	12.43	148.54	12.08	0.0204	1.2193	0.2942	1.0000
O K	0.65	1.07	47.47	11.73	0.0052	1.1402	0.7065	1.0000
SiK	83.30	77.74	3229.19	5.53	0.8258	0.9906	0.9992	1.0017
P K	10.36	8.77	225.25	7.86	0.0898	0.9453	0.9172	1.0004

Table 4 shows data of an example measurement of the carbon concentration using SEM/EDS.. Except for carbon and silicon, oxygen and phosphorus can also be detected. Existence of O can be attributed to the oxidation of deposited a-SiC$_x$:H, the existence of P is due to the doping by PH3. Z, A, F were used in matrix correction to describe the influence of different compositions in the sample to the intensity of X-ray. Z, A, F refer to the atomic number correction, the absorbance correction, and the correction, respectively [87]. As can be seen from Figure 32, the carbon concentration increases with higher methane flow fraction and a higher power density. The increase of carbon concentration concerning the increase of methane flow fraction can be easily understood when using a higher methane concentration in the chamber. The increase of the carbon concentration with higher deposition power can be explained by the stronger chemical bonds of CH_4 compared to that of SiH_4, hence a higher deposition power enhances the dissociation of CH_4 molecules, resulting in a higher carbon concentration in the sample.

3.1.4 Porosity as a function of methane flow fraction and power density

The porosity of each sample was calculated based on their refractive index measured from spectroscopic ellipsometry. It is also necessary to know the carbon concentration of each sample, to calculate the refractive index of the bulk material (with porosity) under a specific composition.

Bruggeman Effective Media Approach was applied to translate the measured refractive index to

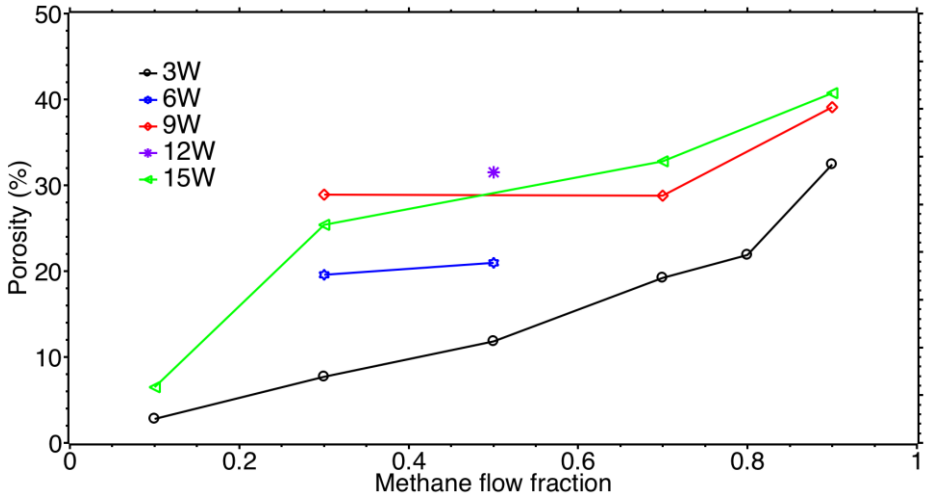

Figure 33. Porosity as a function of methane flow fraction and deposition power

porosity. It can be seen from Figure 33 that the porosity of each sample increases with a higher methane flow fraction, because with a higher methane flow fraction, more CH_4 molecules will be dissociated and involved in the reaction, resulting in a higher concentration of CH_3 groups. In general, the porosity also increases with a higher deposition power from 3W to 12W, while from 12W to 15W it more or less stabilized. This increase in porosity can be related to both the higher carbon concentration (more CH_4 dissociation) and the higher deposition rate with increased deposition power.

3.1.5 Example of conductivity measurements

Three samples were measured, Sample 1 with 1.13% carbon concentration, 0.30 porosity has a conductivity of 2.16 x 10^{-4} S/m, Sample 2 with 0.62% carbon concentration, 0.12 porosity has a conductivity of 6.16 S/m, while Sample 3 with 16.12% carbon concentration, 0.39 porosity has a conductivity of 4.48 x 10^{-10} S/m.

It can be seen that those three samples have a very large difference in porosity and carbon concentration. Sample 1 with the lowest carbon concentration and porosity has the highest conductivity, while in Sample 3 the increase in carbon concentration of nearly 15% increased significantly the bandgap of the sample from 1.584 to 1.944 (activation energy also increased from barely detectable to 726 meV), and resulted in a much lower conductivity.

3.2 Porosity as a function of carbon concentration

Now the relationships between carbon concentration and refractive index, refractive index and porosity have been obtained, the relationship between the porosity and the carbon concentration for each sample can be derived. This relationship is shown in Figure 34. It can be seen that the porosity of the deposited film increased with a higher carbon concentration and

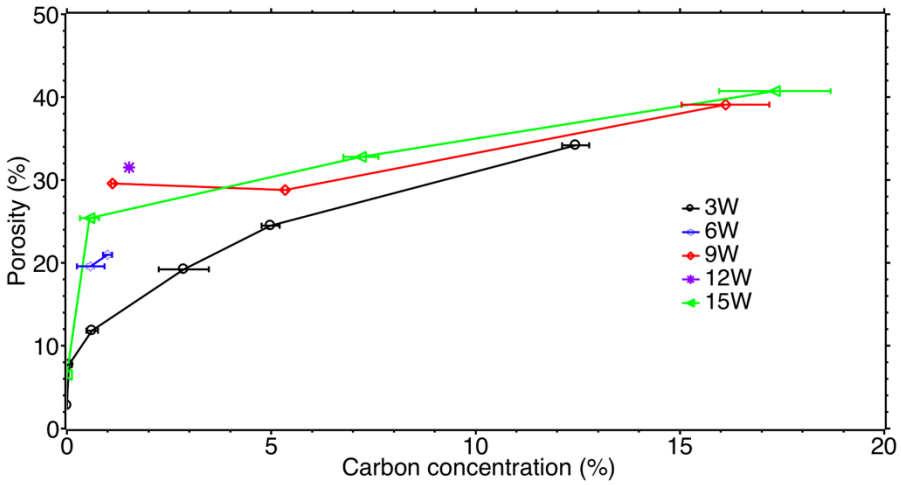

Figure 34. Porosity as a function of carbon concentration.

deposition power. Using Figure 34 allows the influence of porosity and carbon concentration on the performance of the battery to be disentangled. For example, in Figure 34 two samples with the same carbon concentration but different porosity, or with the same porosity but different carbon concentration can be chosen. By comparing the battery performance between those samples, the role of porosity and carbon concentration can thus be investigated separately.

We can see that in the low carbon concentration region (carbon concentration from 0% to 5%), a slight change in carbon concentration results in significant changes in porosity, while at higher carbon concentration region (carbon concentration from 5% to 20%), the porosity does not vary so strongly with carbon concentration.

The trend shows that all curves could be intersecting near 17% carbon concentration, 40% porosity. The difference between each curve could be more pronounced at even higher carbon concentration region, however, a higher carbon concentration may require changes in other deposition parameters, such as a higher chamber pressure or a higher temperature.

4. Results for battery tests of a-SiC$_x$:H

In this chapter, the results of battery tests will be presented. First, the test conditions and the results for pouch-cell tests will be shown. Then the testing strategy and results for coin-cell samples with a low mass load. This is followed by the results for coin-cell samples with higher mass load. For each part, the influence of porosity and carbon concentration on battery performance, such as specific capacity, Coulombic efficiency, and potential change during the first cycle discharge will be compared and discussed between different samples. Finally, the influence of the mass load on battery performance will be discussed.

4.1 Testing and condition and results for Pouch-cell tests

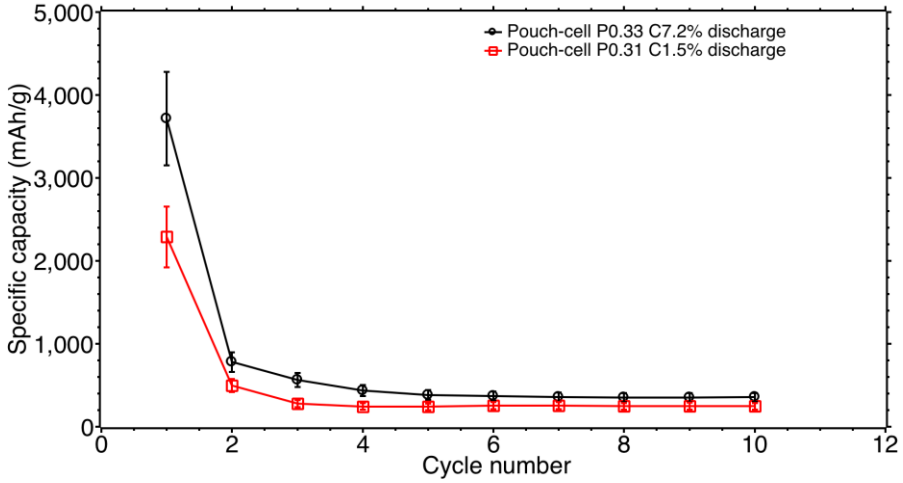

Figure 35. The specific capacity of the discharge as a function of cycle number for Pouch-cell P0.33 C7.2% and Pouch-cell P0.31 C1.5% (P0.33 means the porosity of the sample is 0.33, C7.2% means the carbon concentration of the sample is 7.2%).

4.1.1 Pouch-cell testing condition

Two samples were deposited under *P* = 15W, R = 0.7 and *P* = 12W, R = 0.5, with carbon concentration of 1.52% and 7.15%, porosity of 31% and 32% respectively (properties obtained based on characterization that will be illustrated in later sections). The deposited area was 2 cm x 10 cm, and the deposited mass was 6.6 ± 1 mg and 6.3 ± 1 mg for two above-mentioned samples, respectively. This corresponds to a mass density of 0.33 ± 0.05 mg/cm^2 and 0.31 ± 0.05 mg/cm^2 respectively. The theoretical specific capacity was assumed to be 3000 mAh/g (based on experience), based on which 1C rate current was calculated to be 3.96 mA. 1M $LiPF_6$ in EC/DEC (v/v, 1:1) + 2wt.% VC (additive) was used as electrolyte. Battery was charged to 1.0 V and discharged to 0.1 V at 0.1 C, repeated for 10 cycles.

4.1.2 Results and discussion for pouch-cell tests

From battery tests three main information can be obtained for each sample: charge and discharge specific capacity as a function of cycle number, and coulombic efficiency as a function of cycle numbers. Discharging a lithium-ion battery means that Li^+ ions move from the anode to

cathode (for instance, $LiCoO_2$). In this experiment, it corresponds to the process of Li^+ ions moving from the lithium metal to the a-SiC_x:H electrode in which they are inserted.

In the sample labeling, the value comes after P is the porosity of the sample as void volume fraction, while the value after C is the carbon concentration in percentage. As can be seen in Figure 35, during the discharge of the first cycle for Pouch-cell P0.33 C7.2% the specific capacity starts at a value of 3714 mAh/g. This value is proportional to the number of Li^+ ions that can be inserted per gram material (for example, it can be calculated 3714 mAh/g means for 1 g a-SiC_x:H electrode material, 8.34 x 10^{22} Li^+ ions can be inserted).

First cycle discharge is also conventionally referred to as the specific capacity of a battery, which in this case is 3714 mAh/g. Pouch-cell P0.31 C1.5% on the other hand, only has a discharge specific capacity of 2288 mAh/g. Charging of a Lithium-ion battery means Li^+ ions inserted into a-SiC_x:H are extracted out of this material, which is the opposite of what happened during the discharge. During the charge of the first cycle for Pouch-cell P0.33 C7.2%, as can be seen in Figure 36, the capacity arrives at a value of 1188 mAh/g while is only 192 mAh/g Pouch-cell P0.31 C1.5%. This difference between the discharge and charge capacity can be explained by the Li^+ ions consumption mainly due to the irreversible reaction between carbon in a-SiC_x:H and Li^+ ions, and the side reaction in which the Solid-Electrolyte-Interface (SEI) is formed.

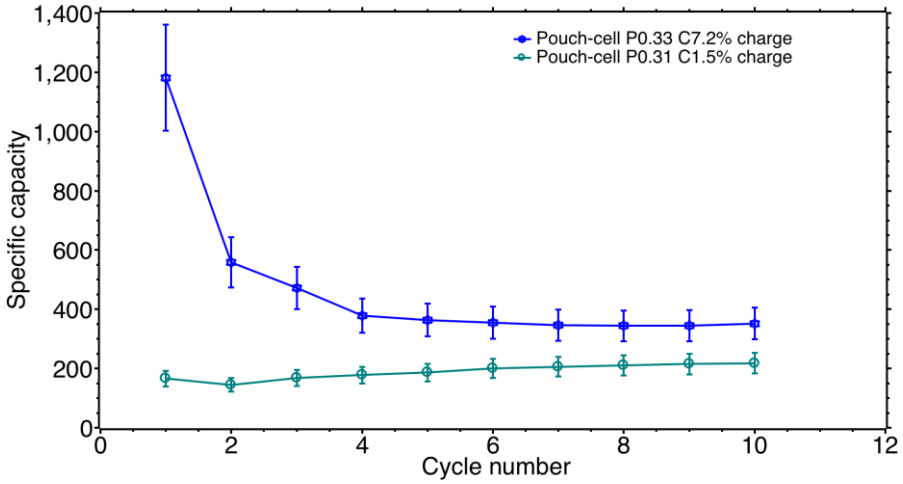

Figure 36. Charge capacity as a function of cycle number for Pouch-cell P0.33 C7.2% and Pouch-cell P0.31 C1.5%.

The term Coulombic efficiency (CE) is used to describe this loss of Li^+ ions. Coulombic efficiency is defined as the first cycle charge (discharge in full-battery tests) capacity divided by the first cycle discharge capacity (charge in full-battery tests) in the half-cell tests. In other words, the amount of recyclable Li^+ ions that are able to be extracted from the a-SiC_x:H electrode during charging divided by the amount of Li^+ ions that are inserted during discharging. As can be seen from Figure 37, the initial Coulombic efficiency which is the first cycle Coulombic efficiency, is the lowest.

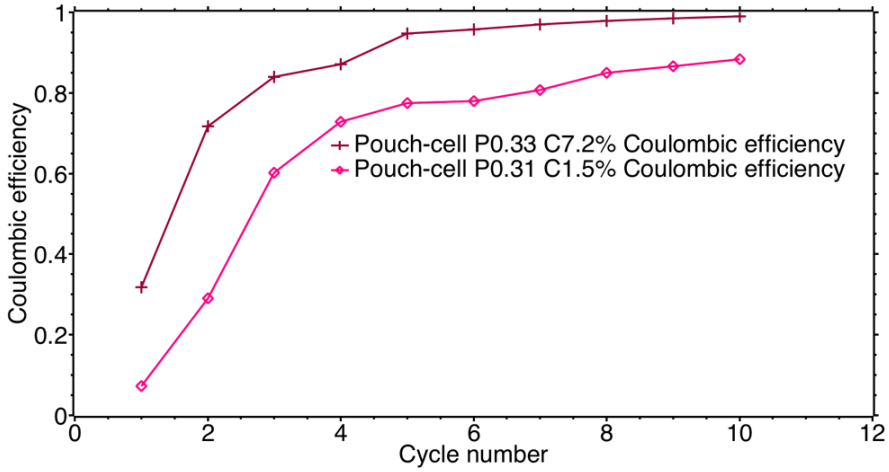

Figure 37. Coulombic efficiency for Pouch-cell P0.33 C7.2% and Pouch-cell P0.31 C1.5%. Based on the equations for error propagation, the error margin for the above mentioned two samples is 21.42%, and 22.81%, respectively.

This is because the irreversible reaction between carbon in a-SiC_x:H and Li^+ ions during the first cycle, and the formation of the SEI layer consumes more Li^+ ions in the first cycle than in later cycles, because the a-SiC_x:H electrode is completely unprotected during the first cycle. Coulombic efficiency will gradually increase after the first cycle and reach 100% when the system is stabilized. Figure 37 shows that Pouch-cell P0.33 C7.2% has an initial Coulombic efficiency of 32% which is significantly higher than Pouch-cell P0.31 C1.5% that only shows an initial Coulombic efficiency of 9%. The Coulombic efficiency of Pouch-cell P0.33 C7.2% reaches 100% after 10 cycles while that of Pouch-cell P0.31 C1.5% only arrives at 82%. From these data, we conclude that for samples deposited on Asahi glass substrates the sample with higher porosity and a higher carbon concentration shows a higher specific capacity and a higher coulombic efficiency than for the sample with lower porosity and carbon concentration.

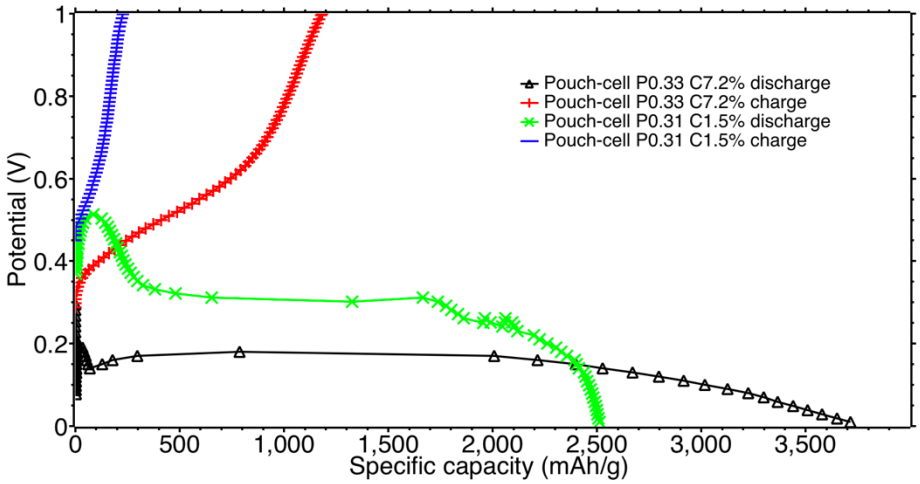

Figure 38. Potential as a function of specific capacity (state of charge) of the first cycle charge and discharge for Pouch-cell P0.33 C7.2% and Pouch-cell P0.31 C1.5%.

Figure 38 shows how the equilibrium potential of the a-SiC_x:H electrode changes as a function of the state-of-charge during both first cycle charge and discharge for Pouch-cell P0.33 C7.2% and Pouch-cell P0.31 C1.5%. It can be seen in the discharge curve for both samples that an increase in potential is observed followed by a decrease during the initial stages the discharge. It is suspected that this peak corresponds to the physical process of Li^+ ions diffusing from the surface deeper into the a-SiC_x:H anode, and that during this process chemical reactions and phase transformations take place in the material [89].

4.2 Testing condition and results for Coin-cell tests

4.2.1 Coin-cell testing condition

Figure 39 shows in total, coin-cell tests were performed for 7 samples (in green cycles). LM-Coin-cell P0.24 C5.0%, LM-Coin-cell P0.32 C12.5% and LM-Coin-cell P0.33 C7.2% were deposited at a lower mass load of around 0.4m/cm^2 and were tested first. Then HM-Coin-cell P0.29 C7.0%, HM-Coin-cell P0.12 C0.6%, HM-Coin-cell P0.33 C7.2%, HM-and Coin-cell P0.39 C16.1% were tested later at a higher mass load of around 1.2mg/cm^2. Figure 39 shows the carbon concentration and

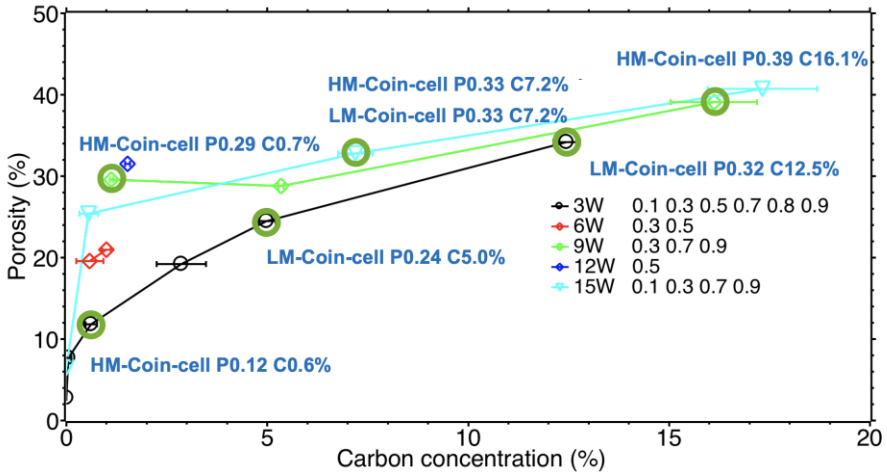

Figure 39. Samples measured for coin-cell battery tests, shown on the map of porosity as a function of carbon concentration.

the porosity of each sample. In the sample's labeling, LM is the short for low mass load; HM is the short for high mass load; P is the porosity, C is the carbon concentration. Those samples were chosen because they have pronounced differences in porosity and carbon concentration between each other.

4.2.2 Results and discussion for coin-cell tests

Areal capacity for samples with low mass load

As can be seen in Figure 40 presents areal capacity as a function of cycle number for LM-Coin-cell P0.24 C5.0%, LM-Coin-cell P0.33 C7.2%, and LM-Coin-cell P0.32 C12.5%. This was calculated directly by dividing the discharge and charge capacity of the electrode by the deposition area for each sample. The black and dark yellow lines at the bottom are the discharge and discharge areal

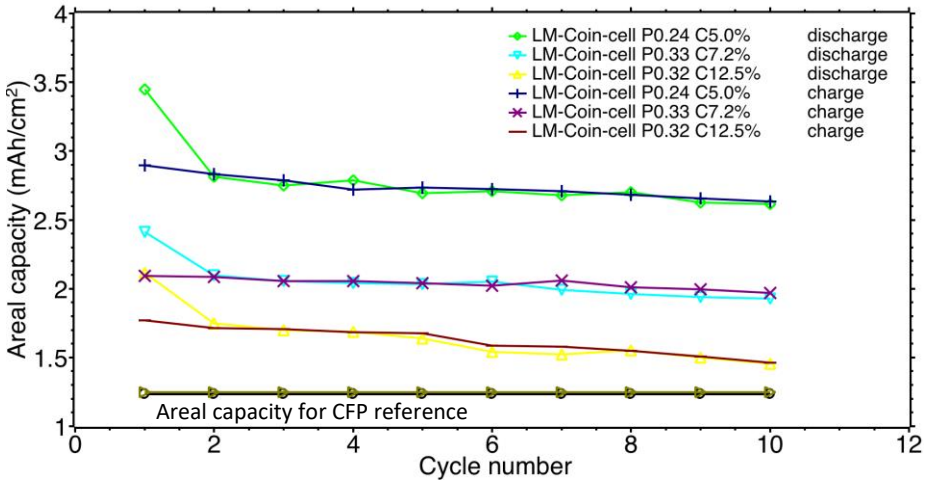

Figure 40.Areal capacity as a function of cycle numbers for LM-Coin-cell P0.24 C5.0%, LM-Coin-cell P0.33 C7.2%, and LM-Coin-cell P0.32 C12.5.

capacity of the CFP reference. They are flat lines since the capacity of the CFP reference does not decrease (or barely decreases) during the first 10 cycles. Because the CFP substrates also can store Li^+ ions, its capacity should be subtracted from the measured capacity to obtain the net capacity of the sample.

Figure 40 shows that three samples show a very significant difference in both discharge and charge areal capacity. Among the three samples, LM-Coin-cell P0.24 C5.0% has the highest areal capacity, which means it absorbs more Li^+ ions during lithiation. This can be explained by the lowest carbon concentration, hence a higher silicon content. LM-Coin-cell P0.32 C12.5% has the highest carbon concentration and shows the lowest areal capacity, while LM-Coin-cell P0.33 C7.2% has a carbon concentration in between and shows an areal capacity in between.

By comparing the areal capacity of LM-Coin-cell P0.33 C7.2% and LM-Coin-cell P0.32 C12.5%, which have almost the same porosity but different carbon concentration, it can be seen clearly how the areal capacity decreases with a higher carbon concentration. When comparing the areal capacity of LM-Coin-cell P0.24 C5.0% and LM-Coin-cell P0.33 C7.2%, although LM-Coin-cell P0.24 C5.0% showed a higher areal capacity, it cannot be concluded whether this is due to the difference in carbon concentration or porosity because they are both different for the mentioned samples.

Specific capacity for samples with low mass load

Although carbon fiber paper (CFP) has many advantages for testing the a-SiC_x:H, we need to take into account that the carbon fibers can also store Li^+ ions, thus also contributes to the capacity. Hence, the capacity of the CFP has to be measured beforehand to be able to work out the capacity of the deposited a-SiC_x: H. Ideally, we would like to use the same current to measure the capacity of the CFP as we measure the sample, which makes the subtraction reasonable. The way we use

to calculate the charge and discharge current of the sample is derived from the following procedure.

1. First we obtain the mass of the sample (mg) by weighing the substrates before and after the deposition. The difference in wight is the mass of the sample.
2. Then the specific capacity of the a-SiC_x:H sample can be obtained by timing the weight of the sample (mg) with its theoretical capacity (mAh/g), which is assumed to be 3000 mAh/g for a-SiC_x:H.
3. If we define the 1 C (mA) that is calculated based on sample mass to be the current at which the battery can be fully discharged in 1 hour, then 0.1 C (mA) is the current we used for charge and discharge.

Meanwhile, the mass load of the sample (mg/cm^2) is obtained by dividing the mass of the sample (mg) by its deposition area (cm^2). A higher mass load also reduces the error brought in by mass measurements.

It can be seen that the charge and discharge current is highly dependent on the mass load of the sample. Hence, ideally we should measure each time the capacity of the CFP substrates with the current calculated based on the mass of each specific deposition. However, due to the time limitation and the limited number of channels for battery tests, we only measured the capacity of CFP substrates using the 0.1 C charge-discharge current based on the sample mass load of 0.3 mg/cm^2.

Hence, when we increased the mass load for LM-Coin-cell P0.24 C5.0% (0.38 ± 0.25 mg/cm^2), LM-Coin-cell P0.33 C7.2% (0.37 ± 0.25 mg/cm^2), and LM-Coin-cell P0.32 C12.5 (0.39 ± 0.25 mg/cm^2) but was still assuming the capacity of the CFP substrates based on the mass load of 0.3 mg/cm^2, it leads to an overestimation of the capacity of CFP reference (a lower mass load leads to a lower charge/discharge current, and consequently a higher capacity) and an underestimation of the

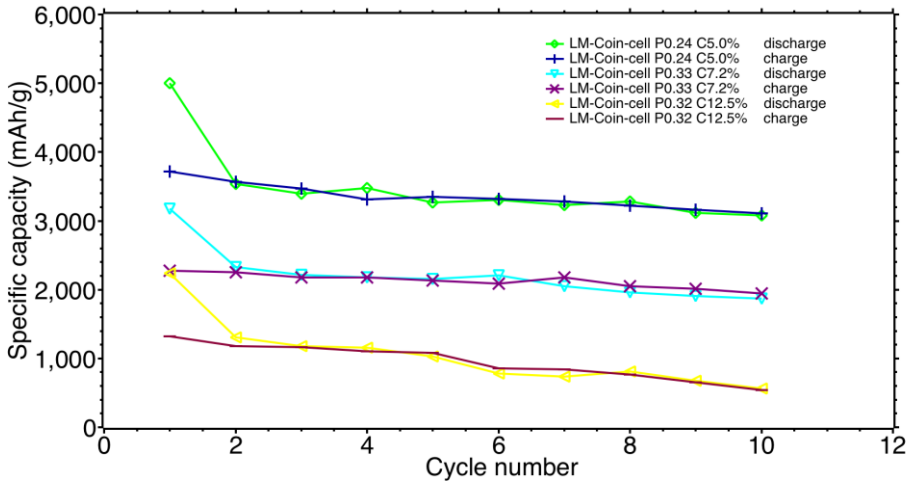

Figure 41. Specific capacity as a function of cycle numbers for samples with a low mass load. The error margin is discussed in the text but not shown in the figure for clarity.

specific capacity of the sample. In the experiments, the capacity of the CFP substrates showed minor fluctuation between each cycle due to the unstable testing condition; hence an average value was taken to represent the capacity of the substrates. Based on the above-mentioned method, the areal capacity was calculated to be 1.26 ± (2.7 x 10^{-5}) mAh/cm^2 .

We can then express the capacity in specific capacity (mAh/g), which is more commonly used in literature. This can be done by dividing the capacity of the a-SiC_x:H by the sample mass. It can be seen that when capacity is expressed in mAh/g, it depends on the mass of the sample. For the mass measurements of LM-Coin-cell P0.24 C5.0%, LM-Coin-cell P0.33 C7.2%, and LM-Coin-cell P0.32 C12.5, the scale with a resolution of 1 mg was used.

The deposition area for all samples was 4cm^2 and based on the measured mass load of 0.38 ± 0.25 mg/cm^2, 0.37 ± 0.25 mg/cm^2, and 0.39 ± 0.25 mg/cm^2 for LM-Coin-cell P0.24 C5.0%, LM-Coin-cell P0.33 C7.2%, and LM-Coin-cell P0.32 C12.5 it can be calculated that the relative error margin of the mass measurements is 65.79%, 67.57%, and 64.10% for three samples, respectively. This means that unfortunately the specific capacity cannot be accurately measured either. As can be seen from Figure 41, the specific capacity for LM-Coin-cell P0.24 C5.0% was nearly 5000 mAh/g, which is higher than the theoretical value of a Si electrode (4200 mAh/g [23]), this is not realistic and can be attributed to the inaccurately measured weight. Although the capacity of LM-Coin-cell P0.33 C7.2% is more reasonable than the other two samples, it is still within a large error margin.

This error brought in by mass measurement will be minimized by increasing the mass load, and by using the scale with a higher resolution (0.1 mg) during the coming battery tests.

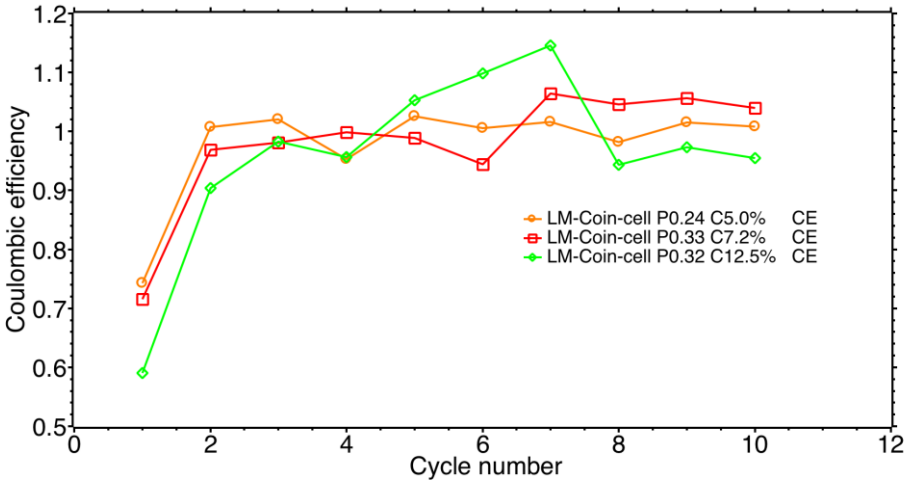

Figure 42. Coulombic efficiency for LM-Coin-cell P0.24 C5.0%, LM-Coin-cell P0.33 C7.2%, and LM-Coin-cell P0.32 C12.5. Based on the equations for error propagation, the error margin for the above mentioned three samples is 92.04%,80.67%, and 80.06%, respectively.

Coulombic efficiency for samples with low mass load

Figure 42 shows the Coulombic efficiency for LM-Coin-cell P0.24 C5.0%, LM-Coin-cell P0.33 C7.2%, and LM-Coin-cell P0.32 C12.5. It can be seen that although they all reach 100% after 3 cycles, they show some differences in initial Coulombic efficiency. LM-Coin-cell P0.32 C12.5 has the lowest initial coulombic efficiency and this can be explained by two reasons:

1. With a higher porosity comes a larger surface area of the electrode, which is a site for side reaction in which forming the SEI layer.
2. With the highest carbon concentration among three samples, the irreversible reaction between carbon in a-SiC_x:H (see in Equation 6) and Li^+ ions will happen to a greater extent, consuming more Li^+ ions. This can be supported by comparing the initial Coulombic efficiency between LM-Coin-cell P0.33 C7.2%, and LM-Coin-cell P0.32 C12.5%, which have virtually the same porosity, but the latter has a higher carbon concentration and a lower Coulombic efficiency.

Although LM-Coin-cell P0.33 C7.2% has a higher porosity and carbon concentration than LM-Coin-cell P0.24 C5.0%, LM-Coin-cell P0.33 C7.2% shows a lower initial Coulombic efficiency. Hence, based on those data it cannot be concluded whether the porosity or the carbon concentration is the dominating factor.

First cycle charge and discharge for samples with low mass load

Figure 43 shows the potential change during discharge as a function of the state-of-charge for the forementioned samples. By comparing this figure with the discharge curves in Figure 38, it can be noticed that the peaks found in the curves for the pouch-cells during the initial stages of the discharge are not observed in Figure 43. These peaks represent the physical process of Li^+ ions diffusing from the surface of the a-SiC_x:H electrode deeper into it, as well as the corresponding chemical reactions and phase transformation. The absence of the peaks suggests that possibly a more amorphous structure of the film was deposited on carbon fiber paper substrates than on glass substrates, providing a faster and easier route for Li^+ ion diffusion.

Areal capacity for samples with high mass load

Due to the high error margin brought in by mass measurements of the sample, another series of samples were deposited under a high mass load in order to reduce this error margin. These samples are HM-Coin-cell P0.29 C0.7%, HM-Coin-cell P0.12 C0.6%, HM-Coin-cell P0.33 C7.2% , and HM-Coin-cell P0.39 C16.1%. Samples are labeled in the same way as the samples with low mass load. HM-Coin-cell P0.33 C7.2% has the same carbon concentration and porosity with LM-Coin-cell P0.33 C7.2% , only the deposition time is longer to increase the mass load. Those four cells are different in three ways compared to previous samples, in order to minimize the error brought in by mass.

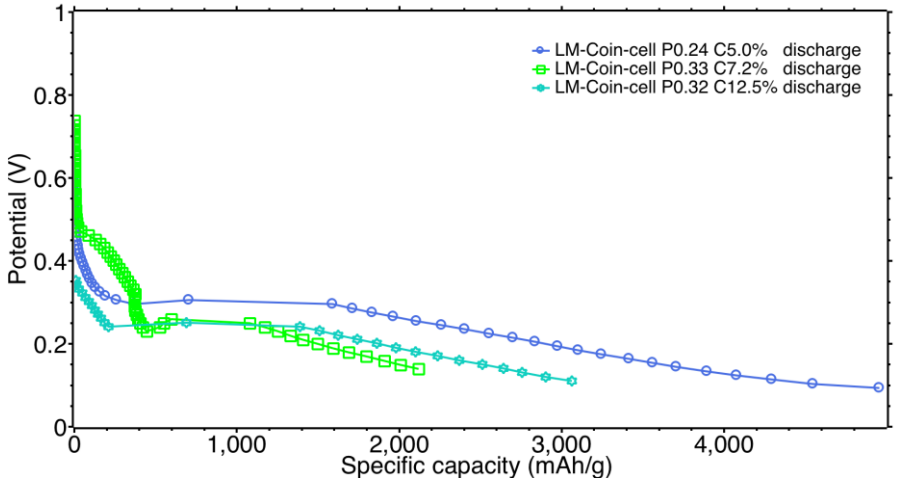

Figure 43 Potential as a function of specific capacity (state of charge) of the first cycle discharge for LM-Coin-cell P0.24 C5.0%, LM-Coin-cell P0.33 C7.2%, and LM-Coin-cell P0.32 C12.5.

1. The sample mass was weighed using a scale with 0.1 mg resolution.
2. The mass load was increased from around 0.4 mg/cm^2 to around 1.2 mg/cm^2
3. The deposition area also increased to 15 cm^2, in order to increase the total mass of the deposited a-SiC$_x$:H.

Hence, the specific capacity in mAh/g can be measured with much higher accuracy for these 4 samples.

First, the areal capacity for four samples is shown in Figure 44. It can be seen that the areal capacity for samples with high mass load is higher compared with that in Figure 40. This is due to the increase in film thickness, resulting in an increase in the active material per unit area. It should also be noted that due to the increase in mass load, 1 C current for charge and discharge was also increased, leading to a more pronounced decrease in specific capacity during the first 10 cycles for samples with high mass load compared to the samples with low mass load. This is shown in Figure 44, where a steeper slope can be observed than in Figure 40.

Specific capacity for samples with high mass load

Specific capacity can be calculated following the procedure discussed in previous sections. The results are shown in Figure 45. It can be seen 4 samples showed a very pronounced difference in the specific capacity. By comparing the specific capacity for HM-Coin-cell P0.29 C0.7% and HM-Coin-cell P0.12 C0.6%, which have similar carbon concentration but a big difference in porosity, it can be seen that a higher porosity leads to a slightly higher capacity. This might be explained by realizing that a large surface area comes with the higher porosity, enhancing the electrode reaction kinetics.

By comparing the specific capacity of HM-Coin-cell P0.29 C0.7%, HM-Coin-cell P0.33 C7.2% , and HM-Coin-cell P0.39 C16.1%, which have similar porosity but a very big difference in carbon concentration, it can be clearly seen how the increase in the carbon concentration leads to a lower capacity. This is simply due to a lower silicon content.

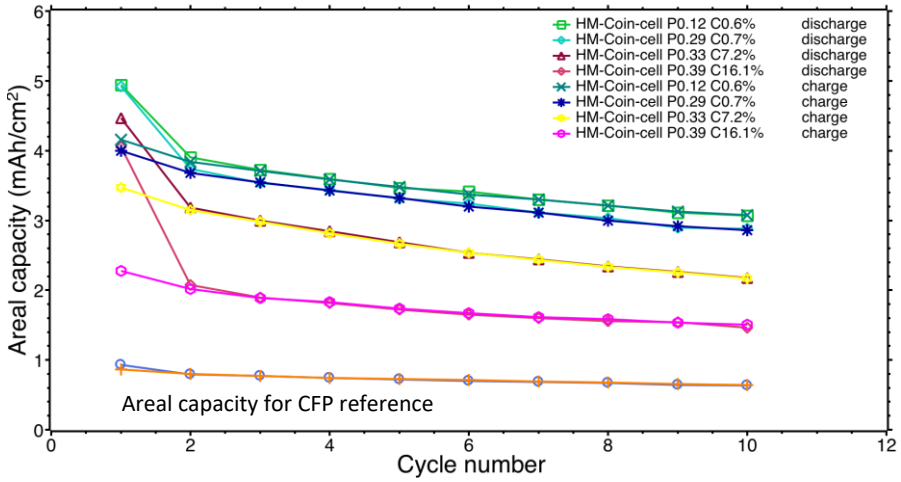

Figure 44. Areal capacity as a function of cycle numbers for HM-Coin-cell P0.29 C7.0%, HM-Coin-cell P0.12 C0.6%, HM-Coin-cell P0.33 C7.2% , and HM-Coin-cell P0.39 C16.1%.

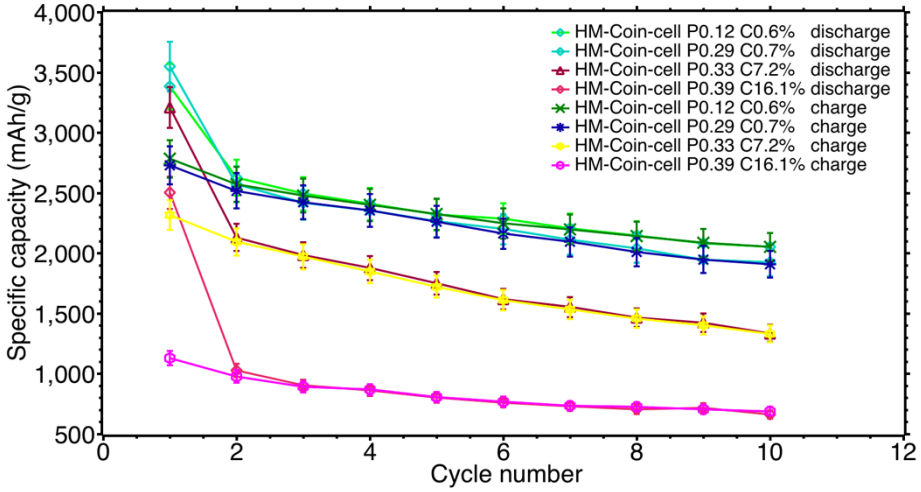

Figure 45. Specific capacity as a function of cycle numbers for HM-Coin-cell P0.29 C0.7%, HM-Coin-cell P0.12 C0.6%, HM-Coin-cell P0.33 C7.2%, and HM-Coin-cell P0.39

For samples with higher mass load, the deposition area is 15 cm^2. The error margin of the mass measurements of HM-Coin-cell P0.12 C0.6% (1.19 ± 0.07mg/cm^2), HM-Coin-cell P0.29 C0.7% (1.15 ± 0.07mg/cm^2), HM-Coin-cell P0.33 C7.2% (1.13 ± 0.07 mg/cm^2), and HM-Coin-cell P0.39 C16.1% (1.25 ± 0.07mg/cm^2) is calculated to be 5.60%, 5.80%, 5.90% and 5.33%, respectively.

Coulombic efficiency for samples with high mass load

Coulombic efficiency can also be compared between samples with high mass load. As can be seen in Figure 46, the Coulombic efficiency for all samples reaches 100% after 2 cycles, but they show some differences in initial Coulombic efficiency. A clear trend can be seen that initial Coulombic efficiency decreases with an increase in carbon concentration. This can be explained by the higher carbon concentration favors the reaction between carbon and Li^+ ions (see in Equation 6).

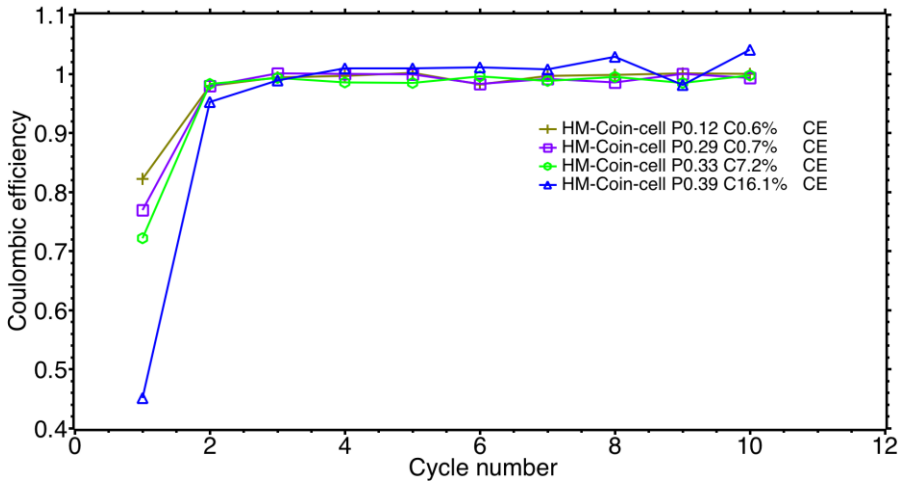

Figure 46. Coulombic efficiency for HM-Coin-cell P0.29 C7.0%, HM-Coin-cell P0.12 C0.6%, HM-Coin-cell P0.33 C7.2%, and HM-Coin-cell P0.39 C16.1%. Based on the equations for error propagation, the error margin for the above mentioned four samples is 8.20%, 7.92%, and 8.34%, and 7.54% respectively.

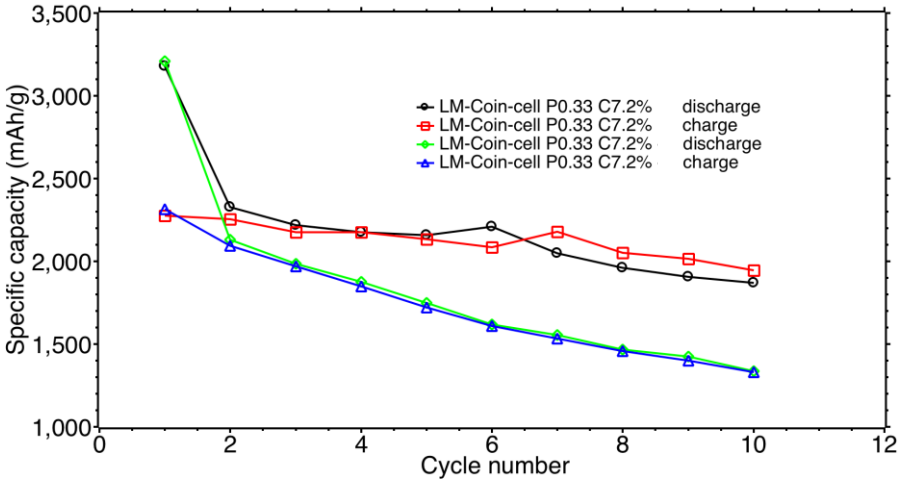

Figure 47. Comparison of the charge-discharge specific capacity for LM-Coin-cell P0.33 C7.2% and HM-Coin-cell P0.33 C7.2%.

Influence of the mass load on battery performance

The mass load of LM-Coin-cell P0.33 C7.2% is 0.37 ± 0.25 mg/cm^2, and that of HM-Coin-cell P0.33 C7.2% is 1.13 ± 0.07 mg/cm^2. By comparing the battery performance of these two samples the

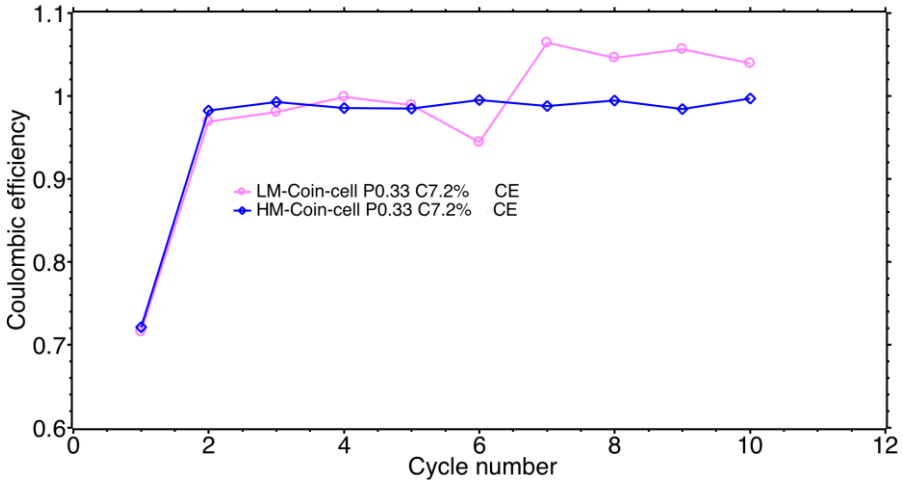

Figure 48. Comparison of the charge-discharge capacity for LM-Coin-cell P0.33 C7.2% and HM-Coin-cell P0.33 C7.2%.

influence of mass load can be shown. A comparison of the charge and discharge specific capacity between 2 samples can be seen from Figure 47. It can be seen that the two samples have very similar charge and discharge specific capacity, indicating that the thickness of the sample does not influence the specific capacity significantly. However, it has to be kept in mind that the error margin for LM-Coin-cell P0.33 C7.2% and HM-Coin-cell P0.33 C7.2% is 65.79% and 5.9%, respectively.

Figure 48 shows the comparison of Coulombic efficiency between two samples. It can be seen both samples have very similar initial Coulombic efficiency and that both reach 100% efficiency. It should be noticed the Coulombic efficiency curve for LM-Coin-cell P0.33 C7.2% shows some fluctuation and with some data points exceeding 100% efficiency. This is because of the unstable test measurement. For example, the temperature rises during the day and drops during the night, as well as the humidity changes. These actors can all lead to the unstable Coulombic efficiency, but we in general regard them as 100%.

It can also be noticed from Figure 47 that although two samples are quite similar regarding both capacity and Coulombic efficiency, HM-Coin-cell P0.33 C7.2% +, with a higher mass load shows a much faster decrease in capacity during the first 10 cycles.

4.3 Discussion for results of the battery tests

In this work, we investigated the influence of carbon concentration and porosity on the capacity fade of a-SiC_x:H electrode. Experiments were carried out to disentangle the influence of the two factors. The most useful information that can be obtained from experiments is the specific capacity (first cycle discharge capacity), and initial Coulombic efficiency.

Huang et al. [22] used 500 nm thick a-SiC_x:H deposited by inductively-coupled- plasma chemical-vapor-deposition (ICP-CVD). This material showed an initial reversible specific capacity 917 mAh/g and 41% capacity remained after 100 cycles at 0.3 C charge/discharge. This is indeed

promising. However, this work only investigated a-SiC_x:H electrode with fixed properties, that is stochiometric a-SiC_x:H (50% carbon concentration) and the porosity was not specified.

Based on the results of our work it is clear that both porosity and carbon concentration play a significant role in the capacity fade of the a-SiC_x:H electrode. For example, a higher porosity leads to a lower initial Coulombic efficiency due to the larger surface area, enhancing the side reaction in which the SEI layer is formed and consuming more Li^+ ions. A higher carbon concentration leads to a lower initial Coulombic efficiency, which is due to the enhanced irreversible reaction between carbon and Li^+ ions. A higher carbon concentration also results in a lower specific capacity (due to a lower Si content). With this relationship between porosity, carbon concentration, capacity, and Coulombic efficiency, we can modify the material properties such that the specific capacity and Coulombic efficiency can be optimized.

The specific capacity of more than 3500 mAh/g presented in our work is higher than reported in literature so far (917 mAh/g in by Huang et al. [22]. The difference is mainly due to the lower carbon concentration used in this work. The highest carbon concentration used in our work is less than 18% while in Huang's work stoichiometric SiC was used). It is also interesting to see that while in Huang's work a higher carbon concentration is used, the initial Coulombic efficiency was as high as 86%, which is even higher than in our work (highest 82%). This is interesting because we conclude from our data that a higher carbon concentration always results in a lower initial Coulombic efficiency. We think that this indicates that other factors influence the capacity fade, such as the porosity.

It was also shown in Huang's work that a decrease in electrode thickness effectively increases the specific capacity by enhancing the electrode kinetics while a thicker film is beneficial for the cycle performance. The explanation for this is that, with a thicker film, more SiC residue remains and serves as a matrix to accommodate the volume expansion. However, the opposite is found in our work. HM-Coin-cell P0.33 C7.2%, with a mass load 3 times as higher (and three times the layer thickness) showed a much faster decrease in specific capacity even at the first 10 cycles comparing to that of LM-Coin-cell P0.33 C7.2%. Meanwhile, the specific capacity between two samples did not show a significant difference (although it must be taken into consideration that the error margin of the specific capacity of LM-Coin-cell P0.33 C7.2% is more than 50%). This might be due to the reason there are different ranges within which thickness has different influences. In the work of Huang et al., the analysis was done for 2 samples with 250 nm and 500 nm thickness, while in this in work, LM-Coin-cell P0.33 C7.2% has a thickness of around 1.2 µm and that of HM-Coin-cell P0.33 C7.2% is nearly 4 µm. However, the exact reason causing this difference is unclear at this point.

Comparison can also be made between a-SiC_x:H in this work and Si anode in previous publications. In the work of Guo's group [90], the specific capacity of a Si anode is indeed higher than a-SiC_x:H, at around 3800 mAh/g, while the initial Coulombic efficiency is around 76%, and is comparable with our work. However, for the Si electrode, the specific capacity drastically decreases to around 1500 mAh/g and 700 mAh/g after 10 and 100 cycles, respectively, corresponding to a Coulombic

efficiency of 40% and 20%, respectively. Despite some differences between samples, in this work the capacity retention is around 70% after 10 cycles, which is much higher than Si anode.

5.COMSOL model

5.1 Introduction

There are several reasons why a-SiC_x:H is potentially an excellent option providing an improved cyclability than Si anode, as explained in Chapter 1. Careful processing of a-SiC_x:H as the anode material has allowed optimization of the porosity and the SiC_x matrix surrounding the pores. The pores are thought to enable the accommodation of the expansion during lithiation, whilst the formation of ductile LiC in the surrounding matrix may manage the expansion. However, 1/10 C charge and discharge rate was adapted for reasons that were explained in Chapter 4, which means 10 hours were needed for both charge and discharge. Including the time needed for the electrode to reach equilibrium potential around 30 hours were needed to complete a whole cycle. Usually, the difference in the capacity fade of a Si-based anode is pronounced after at least 50 cycles [91], which will take approximately 2 months to finish. This is beyond the experimental capacity of this project. To observe the long-term battery performance of a-SiC_x:H anode, and to have a more in-depth understanding of the capacity fade mechanism more optimization opportunities can be provided by computer modeling. With that aim, simulations were performed to be an alternative method and a COMSOL model based on FEM was built, a schematic illustration of which can be seen in Figure 49.

5.2 Model definition

In this work, a 1D model was built using the Lithium-ion battery module in COMSOL 5.4. This modeling was developed based on '1D Lithium-ion battery Model for Capacity Fade' [92] and '1D Isothermal Lithium-Air battery' [93] provided by COMSOL. In this model, mainly three equations are being solved, Equation 13, 14, 15 [94], and the outcome of one equation is used as the input for the next one.

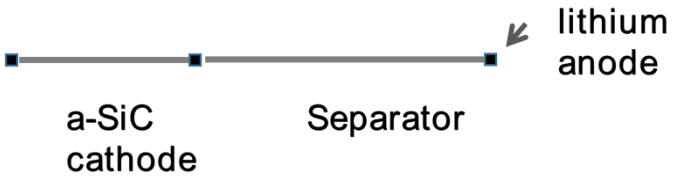

Figure 49. 1D Li-ion battery geometry consisted of cathode made of a-SiC_x:H, separator, and anode made of thin lithium metal foil. This represents a half-cell battery test that we performed in the lab.

$$i_{\mathrm{SEI}} = -(1 + HK)\frac{J i_{\mathrm{loc,1C,ref}}}{exp\left(\frac{\alpha \eta_{\mathrm{SEI}} F}{RT}\right) + \frac{q_{\mathrm{SEI}} f J}{i_{\mathrm{loc,IC,ref}}}} \qquad \text{Equation 13}$$

$$\frac{\partial c_{\mathrm{SEI}}}{\partial t} = -\frac{v_{\mathrm{SEI}} i_{\mathrm{loc,SEI}}}{nF} \qquad \text{Equation 14}$$

$$q_{\mathrm{SEI}} = \frac{F c_{\mathrm{SEI}}}{A_v} \qquad \text{Equation 15}$$

First, the current density of side reaction, i_{SEI} (SI unit: A/m^2) is calculated according to Equation 13 [94]. Then this current density is used to calculate the formation rate of the SEI layer, $\partial c_{\mathrm{SEI}}/\partial t$, which is also proportional to the rate at which Li^+ ions are consumed. Then this rate of Li^+ ions consumption can be used in Equation 15 to calculate the amount of Li^+ ions, q_{SEI} (SI unit: C/m^2), being consumed, which is the capacity loss. This loss in Li^+ ions will in turn influence the current density of side reactions in Equation 18 below and the calculation process is repeated. Symbols and parameters that appear in the model definition are summarized and described in Table 5.

Table 5. Parameters used in model definition.

Symbol	Name / Description	Value	Reference
HK	Dimensionless expansion factor function	200	
J	Dimensionless exchange current density for side reaction	8.4×10^{-4}	[92]
α	Transfer coefficient for electrochemical reduction function	0.56	
η_{SEI}	Overpotential, 0V vs Li/Li^+ is the equilibrium potential	1600 [kg/m^3]	[92]
v_{SEI}	Stoichiometric coefficient of SEI species in the side reaction	250	[92]
n	Number of the electrons participated in the reaction	1	
A_v	Electrode surface area	6.28×10^{-4} [cm^2]	

In the following sections detailed composition and reactions will be discussed for each battery part.

5.2.1 Electrolyte

In this work, the electrolyte consists of $LiPF_6$ in EC/DEC (volume ratio 1:1) and is chosen from the Battery and Fuel Cell/Electrolyte in COMSOL material library. This was the composition we applied in the experiments, although additives such as vinylene carbonate (VC) and fluoroethylene carbonate (FEC) were not taken into account. The concentration of $LiPF_6$ is set to be 1000 mol/m^3, which is also the value used in the experiments. The electrolyte is set to be filled in all domains shown in Figure 49. The diffusion coefficient, electrolyte conductivity, transport number, and activity dependence are all taken as the pre-defined functions provided by COMSOL.

Nernst-Planck equations based on concentrated solution theory are adopted to describe the charge balance in the electrolyte [95].

$$N_+ = \left(-D_2 + \frac{2k_2 t_+ t_- RT}{c_+ z_+ F^2}\right)\left(1 + \frac{\partial \ln f_{\pm}}{\partial \ln c_2}\right)\nabla c_+ - \frac{k_2 t_+}{z_+ F}\nabla \phi_2 \qquad \text{Equation 16}$$

$$N_- = \left(-D_2 + \frac{2k_2 t_-^2 RT}{c_- z_- F^2}\right)\left(1 + \frac{\partial \ln f_{\pm}}{\partial \ln c_2}\right)\nabla c_- - \frac{k_2 t_-}{z_- F}\nabla \phi_2 \qquad \text{Equation 17}$$

In here:

N_+: Positive ion molar flux in electrolyte
N_-: Negative ion molar flux in electrolyte
D_2: Li+ diffusivity in electrolyte
k_2: Ionic conductivity
t_+: Transport number of positive ions
t_-: Transport number of negative ions
c_+: Positive ion concentration
c_-: Negative ion concentration
z_+: Charge number of positive ions
z_-: Charge number of negative ions
$f_\pm$: Average molar activity coefficient
ϕ_2: Electrical potential of electrolyte
$\nabla\phi_1$: Electrical potential of the Si electrode
c_1: Li^+ ions concentration in the Si electrode

And electrolyte current density is expressed as [96]

$$\boldsymbol{i_l} = (-\sigma_1 \nabla\phi_1) + \frac{2\sigma_1 RT}{F}\left(1 + \frac{\partial \ln f}{\partial \ln c_1}\right)(1 - t_+)\,\nabla \ln c_1 \qquad \text{Equation 18}$$

In here:
σ_1: Stress in the Si electrode
$\boldsymbol{i_l}$: Electrolyte current density

5.2.2 Cathode

Since a-SiC_x:H is a novel material for application as the anode in Li-ion batteries, it has not yet been pre-defined in COMSOL at the electrode for simulation. Furthermore, according to SEM/EDS measurements the carbon concentration is relatively low in the deposited samples (with the highest concentration being about 18%, and most below 10%). Hence, as a start to simplify the modeling process, Si is chosen to be the cathode material. By adjusting the properties of the Si electrode in a way it more resembles a-SiC_x:H, the change in porosity and carbon concentration can be simulated. In this way, it is more effective than building new material from the ground.

At the Si electrode, two reactions are simulated.

$$x\mathrm{Li}^+ + \mathrm{Si} + xe^- \rightarrow \mathrm{Li}_x\mathrm{Si} \qquad \text{Equation 19}$$

$$\mathrm{S} + \mathrm{Li}^+ + \mathrm{e}^- \rightarrow \mathrm{P_{SEI}} \qquad \text{Equation 20}$$

In Equation 20, S is the organic solvent in the electrolyte. P_{SEI} is the SEI layer as the product of the reaction.

Li^+ ions insertion and diffusion in Si is described by Fick's law. Chemical reactions between Si and Li^+ ions are described by the Butler Volmer equation [97].

$$i_{1,2} = -i_{Si}\left\{exp\left(\frac{\alpha_a \eta F}{RT}\right) - exp\left(\frac{(-\alpha_c)\eta F}{RT}\right)\right\} \quad \text{Equation 21}$$

$$i_{Si} = Fk_0 c_2^{\alpha_a}\left(c_{theory} - c_{surf}\right)^{\alpha_a} c_{surf}^{\alpha_c} \quad \text{Equation 22}$$

$$\eta = \phi_1 - \phi_2 - U \quad \text{Equation 23}$$

$i_{1,2}$: Transfer current density at Si/electrolyte interface
i_{Si} : Exchange current density at Si/electrolyte interface
α_a : Negative charge transfer coefficient
α_c : Positive charge transfer coefficient
η : Over-potential
k_0 : Reaction rate constant
c_{theory} : Theoretical maximum Li concentration in Si
c_{surf} : Li concentration at the Si surface
ϕ_1 : Electrical potential of Si
ϕ_2 : Electrical potential of electrolyte

The reaction between SiC and Li^+ ions has not yet been included in the model. The reaction requires more complex boundary conditions and mechanical analysis, and although it is of interest of this research, it was beyond my capability and has to be perfected.

5.2.3 Anode

A thin lithium metal foil is used as the anode in this model, as was done in the experiments. At the anode the following reactions mainly occur.

$$Li^+ + e^- \rightarrow Li \quad \text{Equation 24}$$

$$Li \rightarrow Li^+ + e^- \quad \text{Equation 25}$$

The reaction kinetics can be again expressed also by Butler-Volmer equation:

$$i_{loc} = i_0\left(exp\left(\frac{\alpha_a F\eta}{RT}\right) - exp\left(\frac{-\alpha_c F\eta}{RT}\right)\right) \quad \text{Equation 26}$$

$$i_0 = F(k_a)^{\alpha_c}(k_c)^{\alpha_a}\left(\frac{c_1}{c_{1,\,\mathrm{ref}}}\right)^{\alpha_a} \quad \text{Equation 27}$$

The potential of the anode is set initially to be 0 V.

5.2.4 Boundary conditions

No flux

Charged species (Li^+ ions) cannot move through the current collector at the left and right boundaries, so a no-flux boundary condition is applied between the Si electrode and the current collector.

$$N_+ = N_- = 0 \qquad \text{Equation 28}$$

Insolation

As electrons do not enter electrolyte, all boundaries and interfaces of the electrolyte were applied with insolation boundary condition. $\vec{\boldsymbol{\imath}_l}$ and $\vec{\boldsymbol{\imath}_s}$ are two vectors, representing the current at the electrolyte and electrode surface, respectively. $\vec{\boldsymbol{n}}$ is the normal vector in the direction perpendicular to the electrolyte and electrode surface. The insulation boundary condition can then be expressed by the following equations:

$$-\vec{\boldsymbol{n}} \cdot \vec{\boldsymbol{\imath}_l} = 0 \qquad \text{Equation 29}$$

$$-\vec{\boldsymbol{n}} \cdot \vec{\boldsymbol{\imath}_s} = 0 \qquad \text{Equation 30}$$

Charge and discharge cycling

Charge and discharge cycling boundary condition is applied for the Si electrode, simulating the charge and discharge process for different number of cycles. In this boundary condition, the charge and discharge current can be specified. It can also be specified whether to charge or discharge first.

Electrode surface

The electrode surface is applied to simulate the lithium metal anode, because lithium metal foil is highly conductive for electrons and for the diffusion of Li^+ ions, to an extent that the thickness can be ignored. Thus an electrode interface can be used as a representation. Below in Table 6 is a summary of parameters used in the model

Table 6. summary of parameters used in the model.

Symbol	Name / Description	Value	Reference
L_neg	Length of the Si electrode	5×10^{-6} [m]	
L_sep	Length of the separator	30×10^{-6} [m]	
E_max	Maximum potential of Si electrode	0.8 [V]	[98]
E_min	Minimum potential of Si electrode	0.05 [V]	[98]
CS_neg	Maximum Li^+ concentration in Si electrode	2780000 [mol/m^3]	[92]
rp_neg	Radius of Si particle	2×10^{-6} [m]	[99]
t_factor	Time acceleration factor	100	
$Cs_{,initial}$	Initial Li^+ concentration in Si electrode	10000	[92]
M_SEI	Molar mass of product of side reaction	0.16 [kg/mol]	[92]
Kappa	SEI layer conductivity	5×10^{-6} [s/m]	[92]
Rho_SEI	Density of product of side reaction	1.6×10^3 [kg/m^3]	[92]
Dfilm_0	Initial SEI thickness	1 nm	[92]
D_{Si}	Diffusion coefficient of Li^+ in Si	1×10^{-12} [m^2/s]	[92]
α_a	Anodic transfer coefficient	0.5	[92]
α_c	Cathodic transfer coefficient	0.5	[92]
i_{0Si}	Exchange current density of Si lithiation reaction	1×10^{-3} [A/m^2]	[92]
cl	Electrolyte salt concentration	1000 mol/m^3	[92]
K_a	Anodic rate constant of lithium insertion	2×10^{-11} [m/s]	[92]
K_c	Cathodic rate constant of lithium insertion	2×10^{-11} [m/s]	[92]

5.3 Simulation results

After the model was built, it is of our interest to validate the results of simulation by experimental data. In order to speed up the simulation, a time step is pre-defined as the time acceleration factor. The value of the time acceleration factor is equal to the number of cycles simulated per simulation step in the model. Hence, the higher this number, the quicker the simulation will be, but more details will not be captured. It is especially troublesome that the information for the first few cycles (number of cycles equals to the time acceleration factor) will be completely lost, since it is recognized as the first cycle by COMSOL.

Despite my attempts trying to lower this factor, we have not manage to make it lower than 30 without the system reporting errors. When the time acceleration factor is 30, on one hand, it means the simulation is relatively quick and can in general be done within 120 seconds. One the other hand, it also means the information of capacity fade during the first 30 cycles is not captured. Hence, this model still cannot be validated by the experiments. However, it does provide indicative information of how changes in carbon concentration and porosity influence the life time of the electrode.

5.3.1 Influence of porosity

As a start, porous Si electrode was simulated. This model focuses on how the capacity of the electrode decreases with cycle numbers, and how this relationship is affected by the porosity

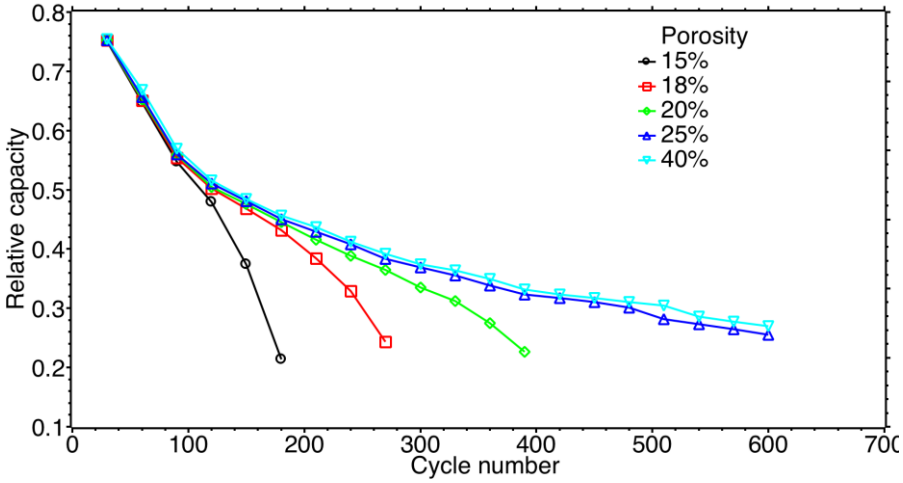

Figure 50. Simulation result of the influences of porosity on the relative capacity fade as a function of the number of discharge-charge cycles.

In COMSOL, porosity is defined as the volume fraction of electrolyte in the electrode (as electrolyte can only be present in pores). This can be changed quite easily by varying the value of the parameter epsl_neg, that is, the porosity. As can be seen from Figure 50, the relative capacity of the electrode (defined as the discharge capacity of each cycle divided by the first cycle discharge capacity) decreases with more cycles, and the speed of decrease is dependent on the porosity. Note that the simulation starts from the 30th cycle. This is controlled by the time acceleration factor. However, our experiments indicate that during the first 10 discharge-charge cycles the decrease in capacity occurs mostly between the first and the second cycle.

Parameters were fitted such that the relative capacity is 75% at the 30th cycle, as is based on a literature finding [100]. It can be seen that a lower porosity comes with a faster decrease in capacity. This can be explained by taking into account that, with lower porosity less space is provided to accommodate the volume expansion during lithiation, leading to cracks in the electrode that will propagate faster and result in electrode failure. In the low porosity region, that is, between 15% and 20%, 1% change in the porosity leads to a very significant difference in decrease slope. This is because, in the low porosity region, the existence of pores is more important to accommodate the volume expansion. In high porosity region above 25% the material provides enough space to accommodate the volume expansion and porosity is no longer the limiting factor of capacity fade.

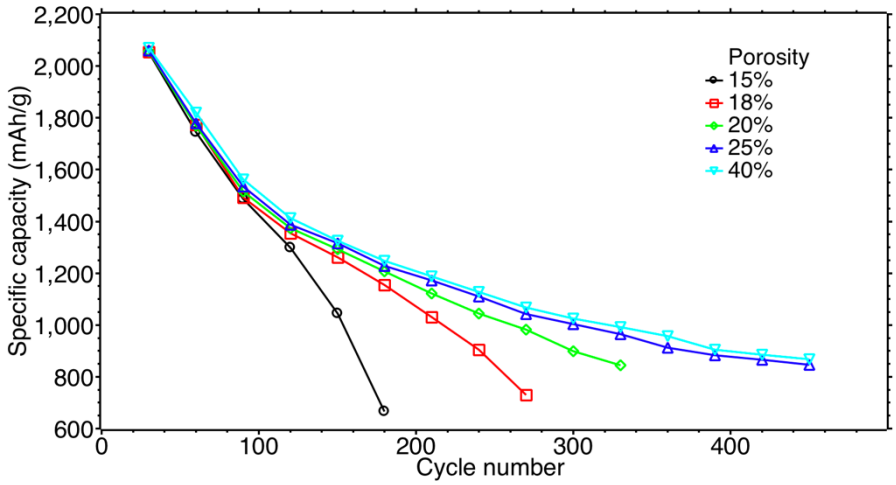

Figure 51. Simulation results of the influences of porosity on the absolute capacity fade as a function of the number of discharge-charge cycles.

Figure 51 shows that the sample with 15% porosity has a specific capacity of 2105 mAh/g after 30 cycles. If we assume that its relative capacity starts from 75% after 30 cycles, an initial capacity of 2800 mAh/g can be calculated. It can also be shown that while porosity differs significantly for each sample, there is not such a big difference in the specific capacity at the 30th cycle. This means that while higher porosity may lead to higher electrode kinetics, it has a less significant influence on specific capacity. In Figure 51, the simulated material with 15% porosity (and 0% carbon concentration since we are simulating a Si electrode so far) resembles the experimental sample LM-Coin-cell P0.12 C0.6% the most. LM-Coin-cell P0.12 C0.6% has a specific capacity of 2051 mAh/g after 10 cycles, as can be seen from Figure 52. Since the decrease in capacity from the 10th to the 30th cycle is expected to be less significant than the first 10 cycles, the capacity of LM-Coin-cell P0.12 C0.6% is not expected to be much lower than 2051 mAh/g at the 30th cycle. This in general matches with the simulation (2105 mAh/g).

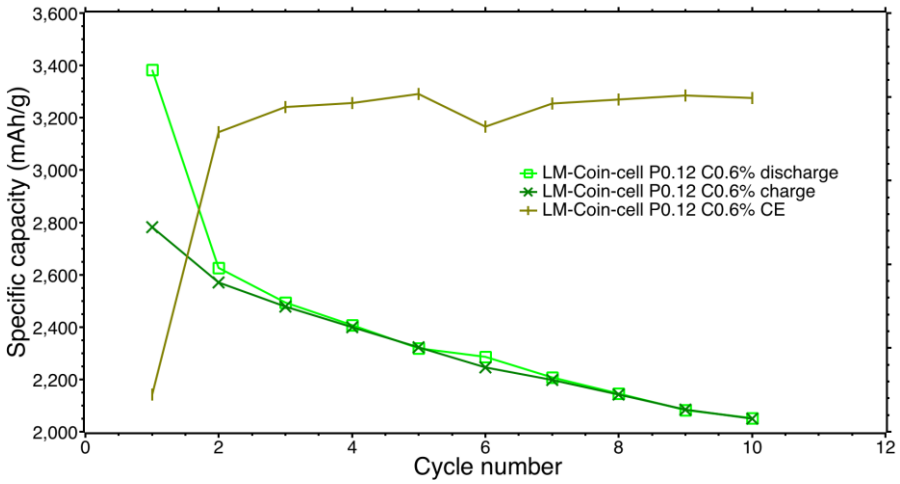

Figure 52 Capacity fade of LM-Coin-cell P0.12 C0.6% as a function of cycle number.

5.3.2 Influence of carbon concentration

It can be seen from the analysis in Section 5.3.1 that the porosity influences the specific capacity and capacity retention ability very significantly. Unlike the change in porosity, in COMSOL there is not a parameter defined as carbon concentration that can be directly changed to simulate the change in carbon concentration. Instead, the change in carbon concentration has to be reflected in multiple other material properties, some of the most important ones are the following. In all the following simulations the porosity was controlled to be 30% to specifically mimic and investigate the influence of carbon concentration.

Volume expansion factor

In Equation 13, K (Volume expansion factor) is the factor that describes the volume expansion of electrode material during lithiation and delithiation. The most pronounced difference between C and Si for electrode application is that for each Li^+ ion adsorbed by Si a much higher volume expansion is realized compared to a Li^+ ion absorbed C.

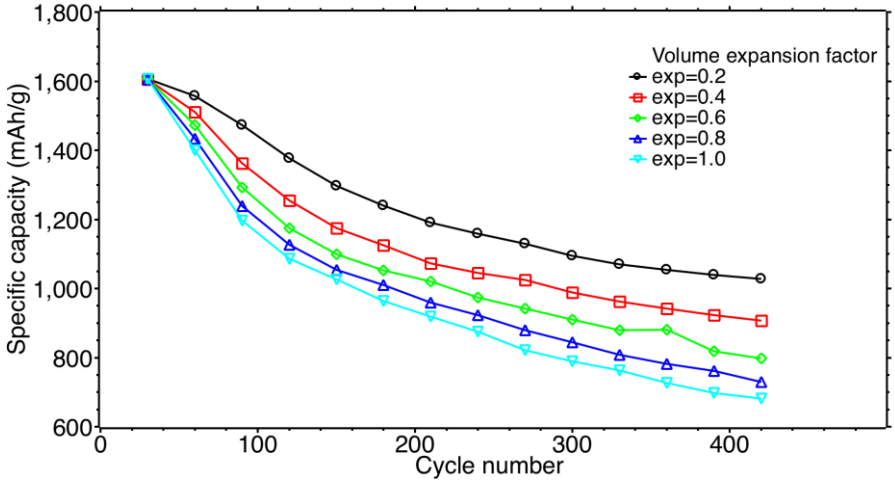

Figure 53. Simulating the change in carbon concentration by varying the value of volume expansion factor.

If we define for a pure Si anode the volume expansion factor K (exp) to be 1 for one inserted Li^+ ion, this value should be lower for the graphite electrode. As can be seen from Figure 53, when decreasing the value of this factor from 1 to 0.2 (represents an increase in carbon concentration), the capacity at the 30th cycle remains virtually the same. Meanwhile, the rate of capacity fade is significantly influenced by the K factor. A higher K factor leads to a faster decrease in capacity. This decrease in capacity is also more pronounced in the lower K region, from 0.2 to 0.6. For higher values of the expansion factor less significant the difference between each value.

Maximum Li^+ ions concentration of the electrode

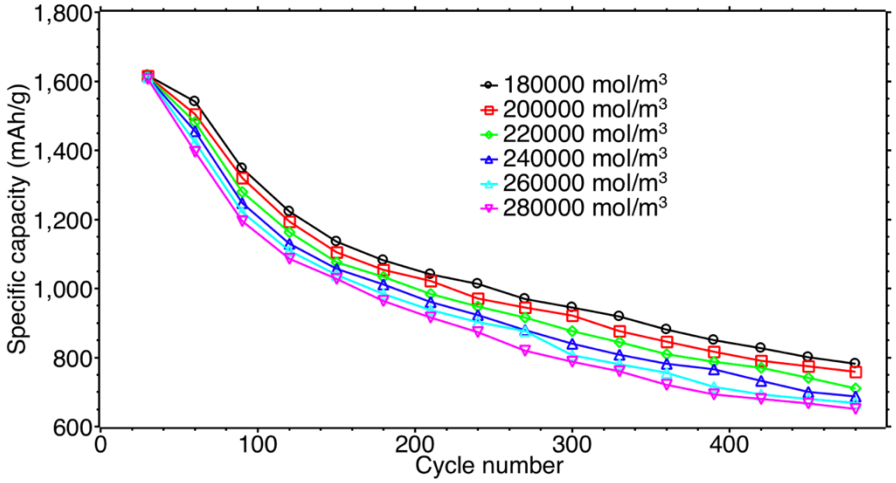

Figure 54. Simulation results of the influence of the maximum Li^+ ion concentration of the electrode on the capacity fade.

It was shown that a Si electrode can accommodate up to 4.4 Li^+ ions per Si atoms, while as many as 6 C atoms can only store 1 Li^+ ion [22]. In other words, C atoms are much less efficient than Si in terms of the number of Li^+ ions can be stored. Consequently, as the carbon concentration increases in a-SiC_x:H, the electrode is less able to store Li^+ ions. This can be reflected by the maximum concentration of the electrode. This value for Si is 278000 mol/m^3 [101], and that of graphite is around 48000 mol/m^3 [92]. A higher carbon concentration is assumed to lower the whole capacity of the electrode. As can be seen from Figure 54 that a variation of maximum concentration influences the rate of capacity fade. With a higher maximum concentration, more Li^+ ions can be accommodated and thus create more expansion.

Diffusion coefficient of the electrode

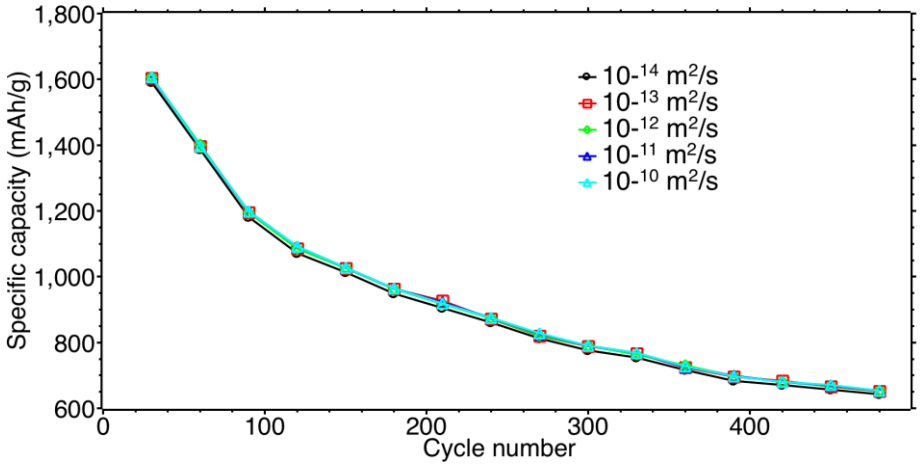

Figure 55. Simulation results of the influence of the diffusion coefficient of Li^+ ions in the electrode on the capacity fade

The diffusion coefficient of Li^+ ions in the electrode also changes with the increase of the carbon concentration. The diffusion coefficient of Li^+ ions in Si is around 10^{-12} m^2/s [92] while that of

carbon was estimated to be around 10^{-13} m^2/s [102], so with an increase of the carbon concentration the diffusion coefficient of a-SiC_x:H should also be lowered. As shown Figure 55, for material with 30% porosity in the simulation the variation of diffusion coefficient from 10^{-14} to 10^{-10} m^2/s does not make a big difference in the cycle performance of the electrode. From this we conclude that the diffusion coefficient of Li^+ in the electrode is not the limiting factor of capacity fade.

5.4 Conclusion for simulation results

In this work, a COMSOL model was established, as a complementary method to show the cycling ability of the electrode, up to 500 cycles. An important advantage of simulation is that the influence of porosity and carbon concentration can be easily separated, unlike in the experiments, where those two properties are more or less interconnected. In the COMSOL model, the variation of porosity can simply be simulated by doing a parametric sweep of electrolyte volume fraction in the electrode. The change in carbon concentration, on the other hand, is more complicated, because this change has to be reflected in the material/electrode properties, such as volume expansion sensitivity towards Li^+ ions insertion, ability to accommodate Li^+ ions, diffusion coefficient, and electrical conductivity, etc. Moreover, changes in those properties happen simultaneously as carbon concentration increases or decreases, which makes it more complicated to relate quantitatively the amount of change in these properties and the change in the carbon concentration. Still, the model is indicative in many ways. First, it presents the information of capacity fade after 30 cycles, which is the region that is not covered yet by experiments. Secondly, it indicates the limiting factors on capacity fade speed, namely, electrode porosity, the number of Li^+ ions stored in the electrode, and the volume expansion created per inserted Li^+. Although some properties can also change as a consequence of changes in porosity and carbon concentration, such as diffusion coefficient, they do not have significant influences on the capacity fade.

It is shown by the model that a higher porosity increases the cycle life of electrode, while does not have a significant influence on the specific capacity. A higher carbon concentration is also beneficial to the cycling ability by reducing the number of Li^+ ions insertion and volume expansion created per Li^+ ion insertion.

6.Conclusion

In this research, both experimental and simulation approaches are applied, together they reveal how porosity and carbon concentration affects different aspects of the electrode performance. It can be concluded that, first, a-SiC_x:H is a functional anode material for Li-ion battery. It can be assembled into a pouch-cell and a coin-cell when deposited on different substrates, and showed promising battery performances: For the sample deposited in carbon fiber paper, with 33% porosity and 7.2% carbon concentration, the specific capacity is 3178 mAh/g and the initial Coulombic efficiency 72%. Secondly, the structure of the deposited a-SiC_x:H films are different when deposited on different substrates. Specifically, a more amorphous structure can be observed on carbon fiber paper substrates than on glass substrates.

Regarding the influence of carbon concentration, it can be concluded that a higher carbon concentration leads to lower specific capacity and a lower initial Coulombic efficiency; meanwhile, the cycle life of the electrode can be extended with an increase in carbon concentration.

Regarding the influence of porosity, it can be concluded by both experiments and simulations that it does not have a significant influence on the specific capacity. On the other hand, a higher porosity results in lower Coulombic efficiency due to the larger surface area of the electrode that comes hand in hand, enhancing the side reaction in which the SEI layers form. Also, the cycle life of the electrode can be extended significantly by an increased porosity, this phenomenon is especially pronounced at the low porosity region (porosity below 20%). While porosity is beyond 25%, the influence of porosity on capacity fade becomes minimal.

Furthermore, we can see that when the thickness of the electrode is between 1-4 μm, it does not have a major influence on the specific capacity and initial coulombic efficiency, while influenced quite significantly the cycle performance: the thicker sample appeared to decrease much faster in capacity at the initial stage, with the capacity retention was 58.8% and 41.6% after 10 cycles for the sample with 1.2 μm and 4 μm thickness, respectively.

7.Outlooks

In this research, due to the limitation of time and battery testing channels, experiments as well as simulations were combined to reveal the influence of porosity and carbon concentration. It will be more persuasive if more cycles can be performed by experiments. This can be done using a higher charge and discharge current, to validate the simulation. It is also interesting to see whether this type of material is stable under higher current.

Also, a more in-depth investigation can be conducted regarding the reaction mechanism of the reaction between a-SiC_x:H and Li^+ ions and how LiC, as a matrix, accommodate the volume expansion. SEM images can be taken to see the change of film structure before and after cycling, this can to some extent, reveal the structural influence of electrode on battery performance.

Regarding the simulation, more reactions (for example, the reaction between carbon and Li^+ ions) should be incorporated in the model to provide a more realistic simulation result. A new approach is needed to establish a relationship between carbon concentration and battery performance, to describes in a quantitatively way what are the influences of carbon concentration. The model can also be completed by adding more functions, such as the ability to simulate not only how carbon concentration and porosity influence the battery performance, but also how different C rate and additives in the electrolyte changes battery performance.

8. References

[1] J. B. Goodenough, "Evolution of Strategies for Modern Rechargeable Batteries," *Acc. Chem. Res.*, vol. 46, no. 5, pp. 1053–1061, 2013.
[2] X. Su *et al.*, "1-s2.0-S0039914013005584-main.pdf," *Adv. Energy Mater.*, vol. 4, no. 1, p. n/a-n/a, 2014.
[3] A. S. Kumbhar, D. M. Bhusari, and S. T. Kshirsagar, "Growth of clean amorphous silicon–carbon alloy films by hot-filament assisted chemical vapor deposition technique," *Appl. Phys. Lett.*, vol. 66, no. 14, pp. 1741–1743, 1995.
[4] I. Renewable and E. Agency, "Renewable Energy Statistics 2020," no. January 2019, p. 408, 2020.
[5] H. Chen, T. N. Cong, W. Yang, C. Tan, Y. Li, and Y. Ding, "Progress in electrical energy storage system: A critical review," *Prog. Nat. Sci.*, vol. 19, no. 3, pp. 291–312, 2009.
[6] C. Liu, Z. G. Neale, and G. Cao, "Understanding electrochemical potentials of cathode materials in rechargeable batteries," *Mater. Today*, vol. 19, no. 2, pp. 109–123, 2016.
[7] M. Thackeray, C. Wolverton, E. I.-E. & Environmental, and undefined 2012, "Electrical energy storage for transportation—approaching the limits of, and going beyond, lithium-ion batteries," *pubs.rsc.org*.
[8] J. B. Kerr, "Advances in Lithium-Ion Batteries Edited by Walter A. van Schalkwijk (University of Washington, Seattle) and Bruno Scrosati (University of Rome, 'La Sapienza'). Kluwer Academic/Plenum Publishers: New York. 2002. x + 514 pp. $120.00. ISBN 0-306-47356-9.," *J. Am. Chem. Soc.*, vol. 125, no. 12, pp. 3670–3671, 2003.
[9] C. De Las Casas and W. Li, "A review of application of carbon nanotubes for lithium ion battery anode material," *J. Power Sources*, vol. 208, pp. 74–85, 2012.
[10] S. Internacional and T. Vedras, "Degradation of Lithium Iron Phosphate-based Cathode in Lithium Ion Batteries : a Post-mortem Analysis," no. January, 2011.
[11] Y. Li, J. T. Han, C. A. Wang, H. Xie, and J. B. Goodenough, "Optimizing Li+ conductivity in a garnet framework," *J. Mater. Chem.*, vol. 22, no. 30, pp. 15357–15361, 2012.
[12] X. Zhang, R. Kostecki, T. J. Richardson, J. K. Pugh, and P. N. Ross, "Electrochemical and Infrared Studies of the Reduction of Organic Carbonates," *J. Electrochem. Soc.*, vol. 148, no. 12, p. A1341, 2001.
[13] K. Xu, "Nonaqueous liquid electrolytes for lithium-based rechargeable batteries," *Chem. Rev.*, vol. 104, no. 10, pp. 4303–4417, 2004.
[14] C. F. Holmes, "Lithium/Halogen Batteries," in *Batteries for Implantable Biomedical Devices*, B. B. Owens, Ed. Boston, MA: Springer US, 1986, pp. 133–180.
[15] V. N. Mitkin, "Types of inorganic fluorocarbon polymer materials and structure-property correlation problems," *Journal of Structural Chemistry*. 2003.
[16] K. Liu *et al.*, "Extending the Life of Lithium-Based Rechargeable Batteries by Reaction of Lithium Dendrites with a Novel Silica Nanoparticle Sandwiched Separator," *Adv. Mater.*, vol. 29, no. 4, pp. 1–6, 2017.
[17] M. S. Whittingham, "Showed That Lithium Self-Diffusion Is," vol. 192, 1976.
[18] J. B. Goodenough, "How we made the Li-ion rechargeable battery: Progress in portable

and ubiquitous electronics would not be possible without rechargeable batteries. John B. Goodenough recounts the history of the lithium-ion rechargeable battery," *Nat. Electron.*, vol. 1, no. 3, p. 204, 2018.

[19] Akira Yoshino and Fujisawa, 1987, Secondary battery, USP4668595.

[20] P. Zhang, Z. Ma, W. Jiang, Y. Wang, Y. Pan, and C. Lu, "Mechanical properties of Li-Sn alloys for Li-ion battery anodes: A first-principles perspective," *AIP Adv.*, vol. 6, no. 1, 2016.

[21] S. N. Kane, A. Mishra, and A. K. Dutta, "Preface: International Conference on Recent Trends in Physics (ICRTP 2016)," *J. Phys. Conf. Ser.*, vol. 755, no. 1, 2016.

[22] X. D. Huang *et al.*, "Electrochemical characteristics of amorphous silicon carbide film as a lithium-ion battery anode," *RSC Adv.*, vol. 8, no. 10, pp. 5189–5196, 2018.

[23] M. Ashuri, Q. He, and L. L. Shaw, "Silicon as a potential anode material for Li-ion batteries: Where size, geometry and structure matter," *Nanoscale*, vol. 8, no. 1, pp. 74–103, 2016.

[24] Y. P. Wu, E. Rahm, and R. Holze, "Carbon anode materials for lithium ion batteries," *J. Power Sources*, vol. 114, no. 2, pp. 228–236, 2003.

[25] https://www.canstockphoto.com/isolated-chiral-carbon-nanotube-10020474.html.

[26] R. Mohamed, S. Ji, and V. Linkov, " Preparation and Characterisation of LiFePO 4 /CNT Material for Li-Ion Batteries ," *Int. J. Electrochem.*, vol. 2011, pp. 1–5, 2011.

[27] G. Maurin, C. Bousquet, F. Henn, P. Bernier, R. Almairac, and B. Simon, "Electrochemical intercalation of lithium into multiwall carbon nanotubes," *Chem. Phys. Lett.*, vol. 312, no. 1, pp. 14–18, 1999.

[28] *Semiconductor Nanomaterials for Flexible Technologies*. 2010.

[29] X. M. Liu *et al.*, "Carbon nanotube (CNT)-based composites as electrode material for rechargeable Li-ion batteries: A review," *Compos. Sci. Technol.*, vol. 72, no. 2, pp. 121–144, 2012.

[30] G. T. Wu, "Structure and Lithium Insertion Properties of Carbon Nanotubes," *J. Electrochem. Soc.*, vol. 146, no. 5, p. 1696, 1999.

[31] J. Wang, I. D. Raistrick, and R. A. Huggins, "Behavior of Some Binary Lithium Alloys As Negative Electrodes in Organic Solvent Based Electrolytes.," *Electrochem. Soc. Ext. Abstr.*, vol. 84–2, pp. 184–185, 1984.

[32] W. C. Maskell, "Cycling Behavior of Thin Film LiAl Electrodes with Liquid and Solid Electrolytes," *J. Electrochem. Soc.*, vol. 132, no. 7, p. 1602, 1985.

[33] T. P. Kumar, R. Ramesh, Y. Y. Lin, and G. T. K. Fey, "Tin-filled carbon nanotubes as insertion anode materials for lithium-ion batteries," *Electrochem. commun.*, vol. 6, no. 6, pp. 520–525, 2004.

[34] Y. Sun *et al.*, "Graphite-Encapsulated Li-Metal Hybrid Anodes for High-Capacity Li Batteries," *Chem*, vol. 1, no. 2, pp. 287–297, 2016.

[35] Y. Xu, D. M. Borsa, and F. M. Mulder, "Engineering the Direct Deposition of Si Nanoparticles for Improved Performance in Li-Ion Batteries," *J. Electrochem. Soc.*, vol. 166, no. 3, pp. A5252–A5258, 2019.

[36] M. Yoshio, H. Wang, K. Fukuda, T. Umeno, N. Dimov, and Z. Ogumi, "Carbon-coated Si as a lithium-ion battery anode material," *J. Electrochem. Soc.*, vol. 149, no. 12, 2002.

[37] C. H. Doh, M. W. Oh, and B. C. Han, "Lithium alloying potentials of silicon as anode of lithium secondary batteries," *Asian J. Chem.*, vol. 25, no. 10, pp. 5739–5743, 2013.
[38] E. Massa, G. Mana, U. Kuetgens, and L. Ferroglio, "Measurement of the lattice parameter of a silicon crystal," *New J. Phys.*, vol. 11, 2009.
[39] Z. Chen, L. Christensen, and J. R. Dahn, "Large-volume-change electrodes for Li-ion batteries of amorphous alloy particles held by elastomeric tethers," *Electrochem. commun.*, vol. 5, no. 11, pp. 919–923, 2003.
[40] Z. Bao *et al.*, "Chemical reduction of three-dimensional silica micro-assemblies into microporous silicon replicas," *Nature*, vol. 446, no. 7132, pp. 172–175, 2007.
[41] A. García, M. Culebras, M. N. Collins, and J. J. Leahy, "Stability and rheological study of sodium carboxymethyl cellulose and alginate suspensions as binders for lithium ion batteries," *J. Appl. Polym. Sci.*, vol. 135, no. 17, pp. 11–13, 2018.
[42] M. Thakur, S. L. Sinsabaugh, M. J. Isaacson, M. S. Wong, and S. L. Biswal, "Inexpensive method for producing macroporous silicon particulates (MPSPs) with pyrolyzed polyacrylonitrile for lithium ion batteries," *Sci. Rep.*, vol. 2, pp. 1–7, 2012.
[43] H. Ma *et al.*, "Nest-like silicon nanospheres for high-capacity lithium storage," *Adv. Mater.*, vol. 19, no. 22, pp. 4067–4070, 2007.
[44] Y. Yao *et al.*, "Interconnected silicon hollow nanospheres for lithium-ion battery anodes with long cycle life," *Nano Lett.*, vol. 11, no. 7, pp. 2949–2954, 2011.
[45] K. Wakabayashi, D. Yamaura, K. Ito, N. Kameda, and T. Ogino, "Fabrication of hollow core-shell type Si/C nanocomposites by a simple process," *e-Journal Surf. Sci. Nanotechnol.*, vol. 15, no. May, pp. 69–73, 2017.
[46] Y. Tanaka, N. Ichimiya, Y. Onishi, and Y. Yamada, "Structure and properties of A1-Ti-Si-N coatings prepared by the cathodic arc ion plating method for high speed cutting applications," *Surf. Coatings Technol.*, vol. 146, no. 147, pp. 215–221, 2001.
[47] R. Cheung, *Silicon carbide micro electromechanical systems for harsh environments*. 2006.
[48] I. Pereyra, C. A. Villacorta, M. N. P. Carreño, R. J. Prado, and M. C. A. Fantini, "Highly ordered amorphous silicon-carbon alloys obtained by RF PECVD," *Brazilian J. Phys.*, vol. 30, no. 3, pp. 533–540, 2000.
[49] K. Daviau and K. K. M. Lee, "High-pressure, high-temperature behavior of silicon carbide: A review," *Crystals*. 2018.
[50] J. B. Casady and R. W. Johnson, "Status of silicon carbide (SiC) as a wide-bandgap semiconductor for high-temperature applications: A review," *High-Temperature Electron.*, vol. 39, no. 96, pp. 511–524, 1998.
[51] G. Brezeanu, "Silicon Carbide (SiC): A short history. An analytical aproach for SiC power device design," *Proc. Int. Semicond. Conf. CAS*, vol. 2, pp. 345–348, 2005.
[52] H. N. Jayatirtha, M. G. Spencer, C. Taylor, and W. Greg, "Single Crystals Grown By the Sublimation Method," vol. 174, pp. 662–668, 1997.
[53] W. Shockley. *Solid-State Electron.*, vol. 2 n°1 (1961) 35-60.
[54] Y. M. Tairov and V. F. Tsvetkov, "Investigation of growth processes of ingots of silicon carbide single crystals," *J. Cryst. Growth*, vol. 43, no. 2, pp. 209–212, 1978.
[55] G. Ziegler, P. Lanig, D. Theis, and C. Weyrich, "Single Crystal Growth of SiC Substrate

Material for Blue Light Emitting Diodes," *IEEE Trans. Electron Devices*, vol. 30, no. 4, pp. 277–281, 1983.

[56] I. H. Kong and N. C, 1991, Homoexpitaxial growth of alpha-SiC thin films and semiconductor devices fabricated thereon, USP5011549.

[57] X. D. Huang, X. F. Gan, F. Zhang, Q. A. Huang, and J. Z. Yang, "Improved electrochemical performance of silicon nitride film by hydrogen incorporation for lithium-ion battery anode," *Electrochim. Acta*, vol. 268, pp. 241–247, 2018.

[58] J. Yang, R. C. De Guzman, S. O. Salley, K. Y. S. Ng, B. H. Chen, and M. M. C. Cheng, "Plasma enhanced chemical vapor deposition silicon nitride for a high-performance lithium ion battery anode," *J. Power Sources*, vol. 269, pp. 520–525, 2014.

[59] A. Mukanova, A. Serikkazyyeva, A. Nurpeissova, S. S. Kim, M. Myronov, and Z. Bakenov, "Understanding the effect of p-, n-type dopants and vinyl carbonate electrolyte additive on electrochemical performance of Si thin film anodes for lithium-ion battery," *Electrochim. Acta*, vol. 330, 2020.

[60] P. A. Savale, "Physical Vapor Deposition (PVD) Methods for Synthesis of Thin Films: A Comparative Study," *Arch. Appl. Sci. Res.*, 2016.

[61] G. Yang, *High-efficient n-i-p thin-film silicon solar cells Guangtao Yang*. 2015.

[62] S. T. Myung, Y. Hitoshi, and Y. K. Sun, "Electrochemical behavior and passivation of current collectors in lithium-ion batteries," *J. Mater. Chem.*, vol. 21, no. 27, pp. 9891–9911, 2011.

[63] D. Wang, W. Liu, X. Zhang, Y. Huang, M. Xu, and W. Xiao, "Review of Modified Nickel-Cobalt Lithium Aluminate Cathode Materials for Lithium-Ion Batteries," *Int. J. Photoenergy*, vol. 2019, 2019.

[64] N. P. Wagner, K. Asheim, F. Vullum-Bruer, and A. M. Svensson, "Performance and failure analysis of full cell lithium ion battery with LiNi0.8Co0.15Al0.05O2 and silicon electrodes," *J. Power Sources*, vol. 437, no. June, p. 226884, 2019.

[65] S. Yoo, C. Hong, K. T. Chong, and N. Seul, "Analysis of pouch performance to ensure impact safety of lithium-ion battery," *Energies*, vol. 12, no. 15, pp. 1–10, 2019.

[66] E. Maiser, "Battery packaging - Technology review," *AIP Conf. Proc.*, vol. 1597, no. February, pp. 204–218, 2014.

[67] C. R. Birkl, E. McTurk, M. R. Roberts, P. G. Bruce, and D. A. Howey, "A Parametric Open Circuit Voltage Model for Lithium Ion Batteries," *J. Electrochem. Soc.*, vol. 162, no. 12, pp. A2271–A2280, 2015.

[68] Q. Si *et al.*, "Carbon paper substrate for silicon-carbon composite anodes in lithium-ion batteries," *J. Power Sources*, vol. 241, pp. 744–750, 2013.

[69] A. Note, "Spectracarb ™ GDL 2050A Series."

[70] W. Zhou, R. Apkarian, Z. L. Wang, and D. Joy, "Fundamentals of scanning electron microscopy (SEM)," *Scanning Microsc. Nanotechnol. Tech. Appl.*, pp. 1–40, 2007.

[71] J. I. Goldstein *et al.*, "Quantitative X-Ray Analysis: The Basics," in *Scanning Electron Microscopy and X-ray Microanalysis*, 2003.

[72] "Helios G4 CX DualBeam System Enabling breakthrough innovations with DualBeam technology-faster and easier than ever before." [Online]. Avaliable:

https://www.thermofisher.com/order/catalog/product/HELIOSPFIBUXE#/HELIOS PFIBUX [73] P. Bulletin, S. Nitride, and I. Eds-ebsd-wds, "Octane Elite EDS System Brochure," pp. 1–2, 2017.

[74] J. A. Wollam, "CompleteEASE™ Data Analysis Manual," Misc, 2008.[Online]. Avaliable: https://www.jawoollam.com/ellipsometry-software/completeease

[75] "J.A Woollam Ellipsometer M-2000 ®," Manual, 2000. [Online]. Avaliable: https://www.jawoollam.com/ellipsometry-software/completeease

[76] N. Yalçin and V. Sevinç, "Studies of the surface area and porosity of activated carbons prepared from rice husks," *Carbon N. Y.*, vol. 38, no. 14, pp. 1943–1945, 2000.

[77] J. Li, L. Wang, X. He, and J. Wang, "Effect of Pore Size Distribution of Carbon Matrix on the Performance of Phosphorus@Carbon Material as Anode for Lithium-Ion Batteries," *ACS Sustain. Chem. Eng.*, vol. 4, no. 8, pp. 4217–4223, 2016.

[78] G. A. Niklasson, C. G. Granqvist, and O. Hunderi, "Effective medium models for the optical properties of inhomogeneous materials," *Appl. Opt.*, 1981.

[79] D. K. Basa, G. Ambrosone, and U. Coscia, "Microcrystalline to nanocrystalline silicon phase transition in hydrogenated silicon-carbon alloy films," *Nanotechnology*, vol. 19, no. 41, 2008.

[80] D. Stroud, "The effective medium approximations: Some recent developments," *Superlattices Microstruct.*, vol. 23, no. 3–4, pp. 567–573, 1998.

[81] A. B. Sproul, M. A. Green, and J. Zhao, "Improved value for the silicon intrinsic carrier concentration at 300 K," *Applied Physics Letters*. 1990.

[82] Ö. Äüôú, "Dielectric Constants of Common Materials," 2003. .

[83] F. Schäffl, "Properties of advanced semiconductor materials : GaN, AlN, InN, BN, SiC, SiGe," *John Wiley Sons Inc New York*, 2001.

[84] Keithley, "6517B Electrometer/High Resistance Meter Datasheet," pp. 1–12.

[85] B. Peri, B. Borah, and R. K. Dash, "Effect of RF power and gas flow ratio on the growth and morphology of the PECVD SiC thin films for MEMS applications," *Bull. Mater. Sci.*, vol. 38, no. 4, pp. 1105–1112, 2015.

[86] J. T. Sagar, S. R. Burgess, C. McCarthy, and X. Li, "Elemental characterisation of sub 20 nm structures in devices using new SEM-EDS technology," *Microelectron. Reliab.*, 2016.

[87] R. C. Reynolds, "Matrix Corrections in Trace Element Analysis by X-Ray Fluorescence: Estimation of the mass absorption coefficient by Compton Scattering," *Am. Mineral.*, 1963.

[88] H. Zhang and H. Xu, "Nanocrystalline silicon carbide thin film electrodes for lithium-ion batteries," *Solid State Ionics*, vol. 263, pp. 23–26, 2014.

[89] C. Liao, Y. Wen, B. Shan, T. Zhai, and H. Li, "Probing the capacity loss of Li3VO4 anode upon Li insertion and extraction," *J. Power Sources*, vol. 348, no. April, pp. 48–56, 2017.

[90] Z. Guo, L. Zhou, and H. Yao, "Improving the electrochemical performance of Si-based anode via gradient Si concentration," *Mater. Des.*, vol. 177, p. 107851, 2019.

[91] J. Sakabe, N. Ohta, T. Ohnishi, K. Mitsuishi, and K. Takada, "Porous amorphous silicon film anodes for high-capacity and stable all-solid-state lithium batteries," *Commun. Chem.*, vol. 1, no. 1, pp. 1–9, 2018.

[92] COMSOL Multiphysics, "Capacity Fade of a Lithium-Ion Battery." [Online]. Avaliable:

https://www.comsol.nl/model/1d-lithium-ion-battery-model-for-the-capacity-fadetutorial-12667.

[93] COMSOL Multiphysics, "1D Isothermal Lithium-Ion Battery Tutorial," pp. 1–32, 2012. [Online]. Avaliable: https://www.comsol.nl/model/1d-isothermal-lithium-ion-battery-686.

[94] H. Ekström and G. Lindbergh, " A Model for Predicting Capacity Fade due to SEI Formation in a Commercial Graphite/LiFePO 4 Cell ," *J. Electrochem. Soc.*, vol. 162, no. 6, pp. A1003–A1007, 2015.

[95] P. Kar and J. W. Evans, "A model for the electrochemical reduction of metal oxides in molten salt electrolytes," *Electrochim. Acta*, 2008.

[96] M. Doyle, T. F. Fuller, and J. Newman, "Modeling of Galvanostatic Charge and Discharge," *J. Electrochem. Soc.*, vol. 140, no. 6, pp. 1526–1533, 1993.

[97] R. Chandrasekaran and T. F. Fuller, "Analysis of the Lithium-Ion Insertion Silicon Composite Electrode/Separator/Lithium Foil Cell," *J. Electrochem. Soc.*, vol. 158, no. 8, p. A859, 2011.

[98] S. Sokhanvaran, A. Danaei, and M. Barati, "Determination of Cell Potential for Silicon Electrodeposition," *Metall. Mater. Trans. E*, vol. 1, no. 2, pp. 187–193, 2014.

[99] C. Graf, D. L. J. Vossen, A. Imhof, and A. Van Blaaderen, "A general method to coat colloidal particles with silica," *Langmuir*, vol. 19, no. 17, pp. 6693–6700, 2003.

[100] S. D. Beattie *et al.*, "Understanding capacity fade in silicon based electrodes for lithium-ion batteries using three electrode cells and upper cut-off voltage studies," *J. Power Sources*, vol. 302, pp. 426–430, 2016.

[101] B. Liu *et al.*, "A Simultaneous Multiscale and Multiphysics Model and Numerical Implementation of a Core-Shell Model for Lithium-Ion Full-Cell Batteries," *J. Appl. Mech. Trans. ASME*, vol. 86, no. 4, 2019.

[102] H. jun GUO, X. hai LI, X. ming ZHANG, H. qiang WANG, Z. xing WANG, and W. jie PENG, "Diffusion coefficient of lithium in artificial graphite, mesocarbon microbeads, and disordered carbon," *New Carbon Mater.*, vol. 22, no. 1, pp. 7–10, 2007.